ARTICLE

doi:10.1038/nature24638

Astrocytic neuroligins control astrocyte morphogenesis and synaptogenesis

Jeff A. Stogsdill[1], Juan Ramirez[1], Di Liu[2], Yong Ho Kim[2], Katherine T. Baldwin[1], Eray Enustun[1], Tiffany Ejikeme[1], Ru-Rong Ji[2,3,4] & Cagla Eroglu[1,3,4]

Astrocytes are complex glial cells with numerous fine cellular processes that infiltrate the neuropil and interact with synapses. The mechanisms that control the establishment of astrocyte morphology are unknown, and it is unclear whether impairing astrocytic infiltration of the neuropil alters synaptic connectivity. Here we show that astrocyte morphogenesis in the mouse cortex depends on direct contact with neuronal processes and occurs in parallel with the growth and activity of synaptic circuits. The neuroligin family cell adhesion proteins NL1, NL2, and NL3, which are expressed by cortical astrocytes, control astrocyte morphogenesis through interactions with neuronal neurexins. Furthermore, in the absence of astrocytic NL2, the formation and function of cortical excitatory synapses are diminished, whereas inhibitory synaptic function is enhanced. Our findings highlight a previously undescribed mechanism of action for neuroligins and link astrocyte morphogenesis to synaptogenesis. Because neuroligin mutations have been implicated in various neurological disorders, these findings also point towards an astrocyte-based mechanism of neural pathology.

Astrocytes actively participate in synapse development and function by secreting instructive cues to neurons[1]. Through their perisynaptic processes, astrocytes maintain ion homeostasis, clear neurotransmitters[2] and contribute to neuromodulatory signalling to control circuit activity and behaviour[3]. These complex functions of astrocytes are reflected in their elaborate structure[4,5], with numerous fine processes that interact closely with synapses. Importantly, loss of astrocyte complexity is a common pathological feature in neurological disorders[6].

Despite the vital functions of astrocytes in brain development and physiology, it is unclear how their complex morphology is established. Furthermore, we do not know whether disruptions in astrocyte morphogenesis lead to synaptic dysfunction. We investigated these questions in the developing mouse primary visual (V1) cortex during postnatal days 1–21 (P1–P21), when astrocyte morphogenesis occurs concomitantly with synaptic development[7,8]. Using Aldh1L1–EGFP BAC-transgenic mice, in which all astrocytes express enhanced green fluorescent protein (EGFP)[9], we found that astrocytic coverage of the V1 neuropil increased profoundly from P7 to P21 (Fig. 1a–c), coinciding with high rates of synaptogenesis[10]. This increase was concurrent with the appearance of fine astrocytic processes (Extended Data Fig. 1a), and only became significant between P7 and P14, when eye opening occurs, suggesting that vision drives this growth (Fig. 1b). Indeed, mice reared in the dark showed profoundly stunted astrocyte coverage of V1 but not of the auditory cortex (Extended Data Fig. 1b–d)

Next, we investigated astrocyte growth at the single-cell level using postnatal astrocyte labeling by electroporation (PALE), which sparsely transfects and labels cortical astrocytes (Extended Data Fig. 1e–h). The volume of fluorescently labelled astrocyte processes infiltrating the neuropil (neuropil infiltration volume, NIV) increased markedly between P7 and P21 (Extended Data Fig. 1i–m). Dark rearing decreased NIV at P21, but not at P7 (Fig. 1d, e). V1 astrocytes also increased their territory size by about 1.6-fold between P7 and P21 (Extended Data Fig. 1n, o). Notably, astrocyte territories were significantly reduced by dark rearing at both ages (Extended Data Fig. 1p, q), suggesting that light-induced changes in V1, which occur even before eye opening[11], are crucial for astrocyte territory growth. Together, our findings reveal that astrocyte morphogenesis occurs in parallel with the growth and activity of the underlying synaptic circuits of the cortex.

To investigate the mechanisms that link astrocyte morphogenesis to neuronal circuit development, we established a primary rat cortical neuron–astrocyte co-culture system, which takes advantage of the observation that astrocyte complexity is greatly enhanced by co-culture with neurons compared to culturing them alone or on Cos7 cells (Extended Data Fig. 2a–e, h). Neuron-conditioned medium was not sufficient to induce astrocyte elaboration (Extended Data Fig. 2e, h). Furthermore, inhibition of astrocyte glutamate sensing by blocking metabotropic glutamate receptor 5 (mGluR5) only slightly impaired astrocyte elaboration, whereas blocking synaptic network activity with tetrodotoxin (TTX) did not diminish neuron-induced astrocyte elaboration (Extended Data Fig. 2f, i). These findings indicate that contact-mediated mechanisms, rather than secreted factors or synaptic activity, are the primary drivers for astrocyte morphogenesis *in vitro*. To test this theory, we fixed neurons with methanol to preserve their structure, while eliminating dynamic feedback to astrocytes. Astrocytes fully elaborated by co-culture with methanol-fixed neurons, whereas methanol-fixed Cos7 cells did not induce elaboration (Extended Data Fig. 2g, j–l). Extraction of neuronal structures with urea, while preserving the deposited extracellular matrix, severely reduced astrocyte elaboration (Extended Data Fig. 2g, j, m). Super-resolution imaging of astrocyte processes and synapses showed that astrocyte elaboration occurs near synapses, and astrocytes interact closely with synaptic structures *in vitro* (Extended Data Fig. 2n). Together, these results show that astrocyte morphogenesis is triggered by direct contact with neurons *in vitro*.

Astrocytes require neuroligins for complexity

Next, we mined gene expression databases[12–14] to identify astrocytic cell adhesion molecules (CAMs) that are known to interact with neuronal and synaptic proteins. Notably, astrocytes express three members of the neuroligin family (NL1, NL2, and NL3) at levels comparable to or higher than those seen in neurons (Extended Data Fig. 3a–f). We confirmed that rodent astrocytes express neuroligins by fluorescent

[1]Department of Cell Biology, Duke University Medical Center, Durham, North Carolina 27710, USA. [2]Department of Anesthesiology, Duke University Medical Center, Durham, North Carolina 27710, USA. [3]Department of Neurobiology, Duke University Medical Center, Durham, North Carolina 27710, USA. [4]Duke Institute for Brain Sciences (DIBS), Durham, North Carolina 27710, USA.

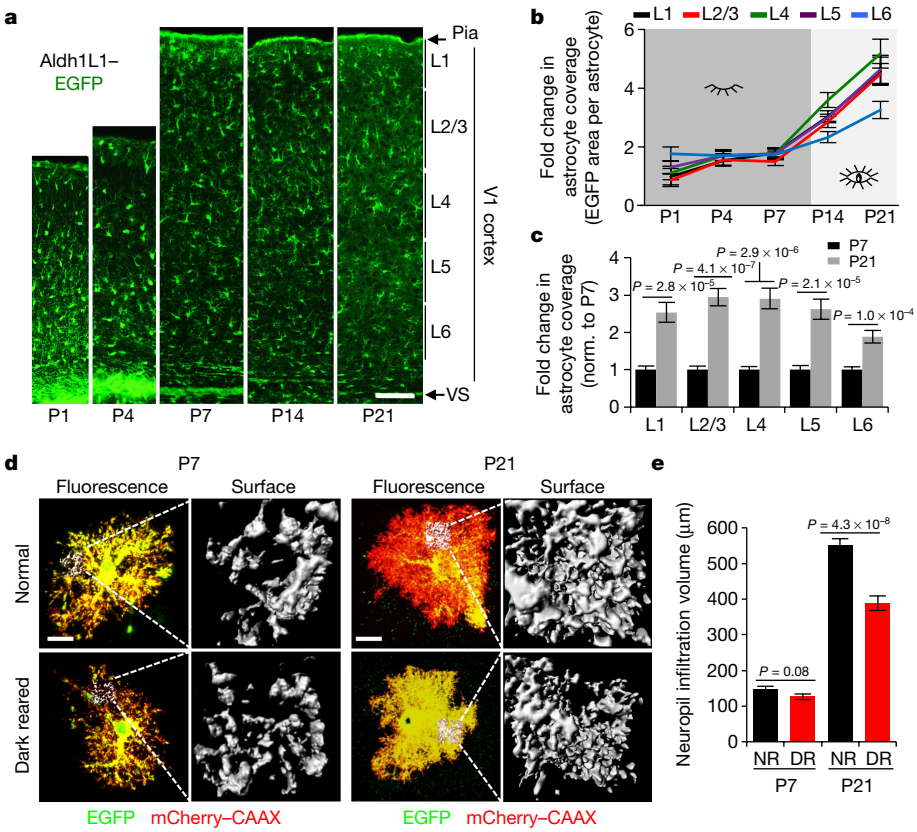

Figure 1 | Astrocyte morphogenesis occurs in tune with sensory activity. a, V1 cortex images (layers L1–L6) from Aldh1L1–EGFP mice at postnatal days P1–P21. **b**, Fold change in astrocyte coverage of the neuropil at each cortical layer from P1–P21 (normalized to P1 L1). **c**, Fold change in astrocyte coverage of the neuropil from P7 and P21 (normalized to P7). **b**, **c**, $n = 10$ regions of interest (ROIs) per layer, more than 3 images per mouse, 3 mice per time point. **d**, Representative images and NIVs of V1 L4 PALE astrocytes from normal (NR) and dark reared (DR) mice at P7 and P21. Astrocytes were electroporated with EGFP (green) and membrane-tagged mCherry (mCherry–CAAX, red) plasmids. **e**, Average NIV of P7 and P21 astrocytes from normal and dark-reared mice. $n = 3$ NIVs per cell, 18–20 cells per condition, 4 mice per condition. One-tailed *t*-test (**c**), one-way ANOVA (**e**). Data are means ± s.e.m. Scale bars, 100 μm (**a**), 10 μm (**d**).

in situ hybridization (FISH) *in vivo* and by PCR with reverse transcription (RT–PCR) and western blotting *in vitro* (Extended Data Fig. 3g–j).

Neuroligins have been mainly studied in the context of neurons[15–17], with few exceptions[18–20]. Simultaneous knockdown of all astrocytic neuroligins with short hairpin RNAs (shRNAs) (Extended Data Fig. 4a) completely blocked neuron-induced astrocyte elaboration *in vitro* (Fig. 2a, b). Silencing each individual astrocytic neuroligin partially but significantly diminished astrocyte arborization, indicating that the neuroligins have non-overlapping roles in astrocyte morphogenesis *in vitro* (Fig. 2a–e, Extended Data Fig. 4d). Co-transfection of neuroligin-targeting shRNAs with the corresponding RNA interference-resistant neuroligin cDNAs[21] (Extended Data Fig. 4b, c) rescued astrocyte elaboration (Fig. 2a, c–e). Knockdown of neuroligins also inhibited astrocyte elaboration induced by co-culture with methanol-fixed neurons (Extended Data Fig. 4e, f). By contrast, knockdown of EphrinA3, a CAM with known roles in astrocyte–neuron interactions[22], did not alter astrocyte morphogenesis (Extended Data Fig. 4g, h). Collectively, these results show that astrocytic NL1, NL2, and NL3 are required for the establishment of neuronal contact-induced astrocyte morphogenesis *in vitro*.

In neurons, neuroligins function by forming trans-synaptic adhesions with neurexins[16]. Swapping the extracellular cholinesterase (ChoE)-like domain of NL1 with the homologous cholinesterase sequence creates a chimaera, NL1-SWAP, that is expressed and trafficked correctly, but cannot interact with presynaptic neurexins[23] (Extended Data Fig. 4i). Co-transfection of NL1-SWAP with an shRNA targeting NL1 (shNL1) failed to rescue astrocyte morphogenesis (Fig. 2f, g), even though shNL1 did not diminish NL1-SWAP expression, and expression of NL1-SWAP alone in astrocytes did not impair astrocyte morphogenesis (Extended Data Fig. 4b, j, k). These results show that contacts mediated by the ChoE-like domain of NL1 are required for astrocyte morphogenesis and suggest that interactions between astrocytic neuroligins and neuronal neurexins regulate astrocyte development.

To test whether neuronal neurexins are required for astrocytic morphogenesis, we silenced neurexin expression in cultured rat neurons using a lentivirus encoding shRNAs against mouse neurexins (Nrx1, Nrx2, and Nrx3 (both α- and β-isoforms[24])). In rat neurons, this lentivirus silenced Nrx1 and Nrx2 but not Nrx3, owing to mismatches between the rat and mouse sequences (Extended Data Fig. 5a–d). Silencing Nrx1 and Nrx2 in neurons significantly diminished neuronal contact-induced astrocyte morphogenesis (Fig. 2h, i). Concurrently silencing NL1 in astrocytes did not further reduce astrocyte complexity (Extended Data Fig. 5e–g), indicating that Nrx1 and Nrx2 are the primary neuronal interaction partners for astrocytic NL1. In addition, these findings suggest that interactions between other astrocytic neuroligins and neuronal neurexins are also important for astrocyte morphogenesis *in vitro*.

Elimination of neuronal neurexins may affect astrocyte morphology independent of the loss of neurexin–neuroligin contacts. To address this possibility, we used methanol-fixed neurons to induce astrocyte morphogenesis and blocked neurexin–neuroligin interactions by applying soluble Fc-tagged Nrxβ ectodomains (Extended Data Fig. 5h–j). Co-application of Nrx1β–Fc, Nrx2β–Fc and Nrx3β–Fc significantly diminished astrocyte complexity compared to Fc-only protein (Extended Data Fig. 5k–m). Application of Nrx1β–Fc or Nrx2β–Fc alone reduced astrocyte elaboration, but Nrx3β–Fc did not (Extended Data Fig. 5n). Meanwhile, silencing astrocytic NL1 did not further diminish astrocyte elaboration (Extended Data Fig. 5o). Next, we tested whether *trans*-interactions with neurexins are sufficient for astrocyte morphogenesis by coating 3D nanofibres with Nrxβ ectodomains to generate an artificial scaffold mimicking a web of neurites (Fig. 2j). Remarkably, all Nrxβ-coated nanofibres strongly induced astrocyte complexity compared to those coated with Fc only (Fig. 2j, k). Together, these results show that interactions with neuronal neurexins are required and sufficient for contact-induced astrocyte morphogenesis *in vitro*.

Neuroligins control astrocyte morphology *in vivo*

To determine whether neuroligins control astrocyte morphogenesis *in vivo*, we introduced EGFP-expressing shRNA plasmids targeting

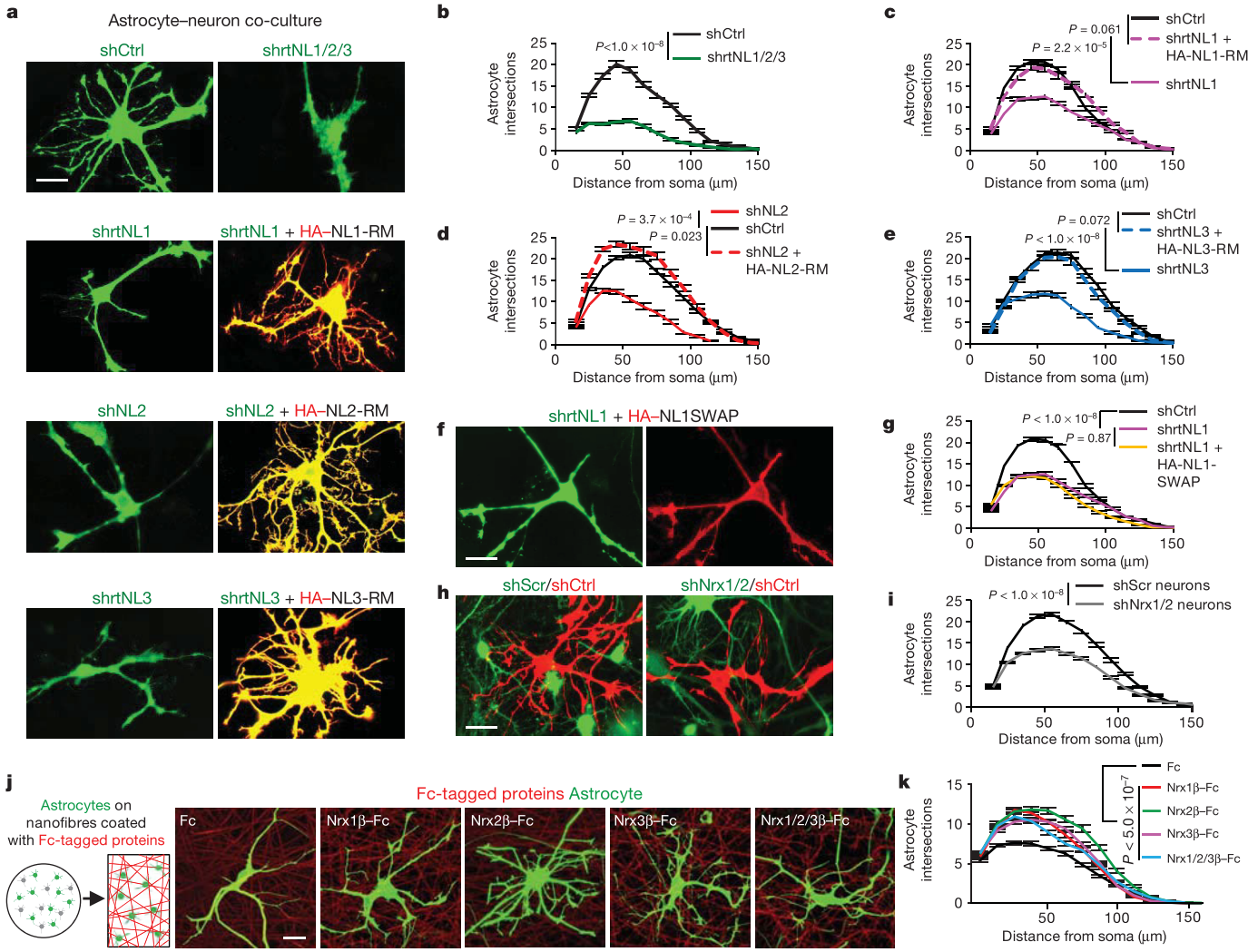

Figure 2 | Astrocytic neuroligins control astrocyte morphogenesis through neuronal neurexins. a, Astrocytes (green) were transfected with shRNAs against rat NL1 (shrtNL1), mouse/rat NL2 (shNL2), and/or rat NL3 (shrtNL3) with or without haemagglutinin (HA)-tagged, shRNA-resistant neuroligin plasmids (red) and co-cultured with neurons (not visible). **b**–**e**, Quantification of astrocyte complexity for conditions in **a**. **f**, Image of an astrocyte transfected with shrtNL1 (green) and HA-tagged NL1-SWAP (red) in co-culture with neurons (not visible). **g**, Quantification of astrocyte complexity for **f**. **h**, Images of shCtrl-transfected astrocytes (red) in co-culture with neurons transfected with shNrx1, shNrx2 or shScr lentivirus (green). **i**, Quantification of astrocyte complexity for **h**. **b**–**e**, **i** Data represented are from individual experiments with three biological replicates. Similar results were obtained in three independent experiments. $n > 20$–25 cells per condition per experiment. **j**, Nanofibres were coated with Fc-tagged proteins to model a neuronal scaffold. Images of EGFP-transfected astrocytes (green) cultured on Fc-protein-coated nanofibres (red). **k**, Quantification of astrocyte complexity for **j**. Data represent one experiment with four biological replicates. $n > 25$ cells per condition. ANCOVA (**b**–**e**, **g**, **i**, **k**). Data are means ± s.e.m. Scale bar, 10 μm.

mouse NL1, NL2 or NL3 into V1 astrocytes by PALE. As a control, we used a scrambled NL1 shRNA sequence (shCtrl, Extended Data Fig. 6a–d). As expected, shCtrl-transfected astrocytes developed main branches by P7 and elaborated finer processes into the neuropil by P21 (Fig. 3a). NL1 knockdown markedly reduced astrocytic NIV at P7, but this was corrected by P21. Conversely, NL3 knockdown did not alter astrocyte morphogenesis at P7, but severely arrested astrocyte growth by P21. Silencing NL2 restricted NIV at both time points (Fig. 3a–f, Extended Data Fig. 6e). These results show that neuroligins are required for astrocyte morphogenesis *in vivo* and suggest that the three neuroligins have unique temporal roles in astrocyte development.

To determine how increasing neuroligin expression alters astrocytic morphogenesis, we overexpressed NL1, NL2, NL3 or NL1-SWAP (control) in astrocytes by PALE. Astrocyte territories were greatly enlarged by overexpression of NL1 or NL2 compared to NL1-SWAP (Extended Data Fig. 6f, g). The NIV of NL1-overexpressing astrocytes did not change, whereas NIV decreased slightly for NL2-overexpressing astrocytes (Extended Data Fig. 6f, h). We were unable to find NL3-overexpressing astrocytes at P21, indicating that NL3 overexpression starting at P1 is not compatible with astrocyte survival and/or maturation. Together, these findings show that neuroligin expression in astrocytes controls neuropil infiltration and territory size of these cells.

Astrocytic NL2 controls synaptogenesis

Because NL2 knockdown markedly impaired astrocyte morphogenesis at P7 and P21, we next investigated the specific *in vivo* functions of NL2 in astrocytes using *Nlgn2*-floxed mice (in which the gene that encodes NL2, *Nlgn2*, is flanked with *lox* sequences)[25]. To address the cell-autonomous effects of NL2 on astrocyte development, we sparsely deleted NL2 by introducing Cre via PALE into $Nlgn2^{+/+}$, $Nlgn2^{f/+}$ or $Nlgn2^{f/f}$ mice (NL2 PALE WT, HET or KO, respectively). These mice also carried a single allele of the $Gt(ROSA)26Sor^{tm14(CAG-tdTomato)Hze}$ (RTM) transgene[26] to label Cre positive (Cre^{+}) cells with td-Tomato expression. NL2 expression in td-Tomato/Cre^{+} astrocytes was greatly diminished, and using these mice and PALE, we confirmed the

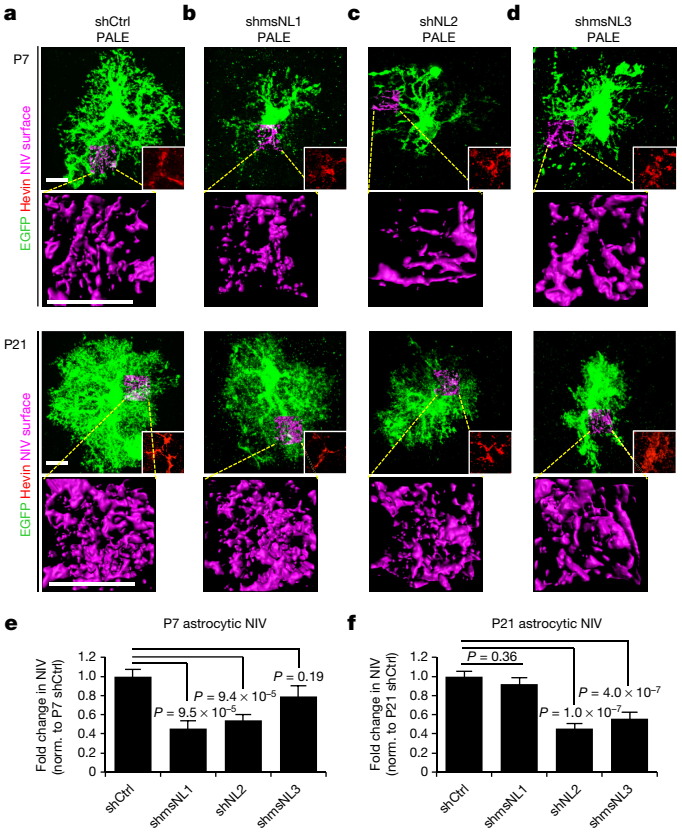

Figure 3 | Neuroligins control the morphological development of astrocytes *in vivo*. **a**–**d**, Representative images of shRNA-transfected L4–5 astrocytes (labelled with EGFP) and NIV reconstructions (magenta) at P7 (top) and P21 (bottom). Astrocytes were electroporated with shRNAs against mouse NL1 (**b**, shmsNL1), NL2 (**c**), NL3 (**d**, shmsNL3) or a scrambled control (**a**, shCtrl). All EGFP$^+$ cells imaged were hevin-positive, confirming their astrocyte identity (red inlay, corresponding to the somatic region). **e**, **f**, Fold change in average NIV for P7 (**e**) and P21 (**f**) astrocytes (normalized to shCtrl). Three NIVs per cell, 10–20 cells per condition, 3 or more mice per condition. One-way ANOVA (**e**, **f**). Data are means ± s.e.m. Scale bars, 10 μm.

specificity and effectiveness of our shNL2 construct (Extended Data Fig. 7a–f). Similar to our results with shNL2 PALE experiments, deletion of NL2 in V1 layer 4 (L4) astrocytes decreased NIV. Loss of a single allele of *Nlgn2* (NL2 PALE HET) was sufficient to cause a partial but significant decrease in astrocyte infiltration (Fig. 4a, b). Furthermore, loss of both *Nlgn2* alleles caused a significant reduction in territory size (Fig. 4c, d). Together, our results show that NL2 has an important function in astrocyte morphogenesis *in vivo*.

Because astrocytes are key controllers of excitatory and inhibitory synaptogenesis[27], we next determined whether astrocytic NL2 is required for proper synaptogenesis. We quantified the synapse density within the territories of NL2 PALE HET and NL2 PALE KO L4 astrocytes and compared it with the density of synapses within the surrounding neuropil infiltrated by WT astrocytes (Fig. 4e). Synapses were labelled by the co-localization of pre- and postsynaptic markers (that is, VGluT1 and PSD95 (intracortical excitatory), VGluT2 and PSD95 (thalamocortical excitatory) and VGAT and gephyrin (inhibitory)). Co-localization of these markers reflects true synapses, as rotating the presynaptic channel by 90° with respect to the postsynaptic channel eliminated most co-localization (Extended Data Fig. 8).

The density of excitatory synapses within the territory of NL2 PALE KO astrocytes was half that of the neighbouring WT astrocytes, whereas loss of a single allele of NL2 did not affect excitatory synapse density within an astrocyte's domain (Fig. 4f–i). Inhibitory GABA (γ-aminobutyric acid)-ergic synapse density was not altered within the domains of NL2 PALE HET or NL2 PALE KO astrocytes (Fig. 4j, k). These results were unexpected and distinct from the known neuronal role of NL2 as a regulator of inhibitory synapse formation[28,29]. We found that astrocytic NL2 is essential for local regulation of synapse development in a cell non-autonomous manner by controlling the formation and/or maintenance of excitatory synapses within the territory of a given astrocyte.

Astrocytic NL2 controls synapse function

To investigate how astrocytic NL2 affects the function of cortical synapses, we conditionally deleted *Nlgn2* (NL2 cKO) in a large population of astrocytes by combining the *Nlgn2* floxed allele containing the RTM transgene with Tg(Slc1a3-cre/ERT)1Nat (GLAST–CreER^{T2}) mice[30]. Cre-recombination was activated by administering tamoxifen at P10 and P11 and monitored by td-Tomato expression (Extended Data Fig. 9a, b). NL2 (but neither NL1 nor NL3) mRNA was significantly reduced in td-Tomato/Cre$^+$ astrocytes isolated from NL2 cKO cortices by fluorescence-activated cell sorting (FACS) compared to littermate NL2 conditional heterozygous (cHET) mice. However, low levels of NL2 mRNA expression were detected, probably owing to incomplete recombination of both floxed alleles in some Cre$^+$ astrocytes (Extended Data Fig. 9a–e). Notably, GFAP expression did not differ between NL2 cHET and cKO astrocytes (Extended Data Fig. 9e), indicating that NL2 cKO cells retained their astrocyte identity and did not undergo pathological reactivation characterized by enhanced GFAP expression[6,31]. Genotyping the sorted cells using allele-specific primers verified the recombination of the *Nlgn2* locus (Extended Data Fig. 9f–i). In V1 visual cortex essentially all td-Tomato/Cre$^+$ cells expressed GFAP, indicating that Cre expression is restricted to astrocytes. By contrast, 58.7 ± 4.0% (mean ± s.e.m.) of the NL2 cHET or 53.9 ± 4.4% of NL2 cKO astrocytes were td-Tomato/Cre$^+$. Deletion of NL2 did not alter the number or distribution of astrocytes or neurons and the td-Tomato signal was absent from neurons within V1 cortex (Extended Data Fig. 10a–e).

We next performed whole-cell patch-clamp recordings of miniature excitatory and inhibitory postsynaptic currents (mEPSCs and mIPSCs, respectively) in V1 L5 pyramidal neurons from P21 NL2 cHET and cKO mice (Extended Data Fig. 10f). L5 neurons possess large dendritic trees that project to all cortical layers and receive extensive excitatory and inhibitory synaptic inputs[32]. The frequency and amplitude of mEPSCs were significantly reduced in NL2 cKO neurons compared to NL2 cHET neurons (Fig. 5a–e). These observations are consistent with our finding that loss of astrocytic NL2 locally decreases excitatory synapse numbers by 50%. Similarly, deletion of NL2 in around 55% of cortical astrocytes reduces the frequency of excitatory synaptic events by about 25%. Together, our data show that astrocytic NL2 is required for the proper formation and function of excitatory synapses in the cortex.

We also detected an increase in the frequency of mIPSCs from NL2 cKO neurons compared to cHET neurons, whereas the amplitudes of mIPSCs were indistinguishable (Fig. 5f–j). The elevated frequency of mIPSCs in NL2 cKO neurons might be mediated by an increase in the number of inhibitory synapses. If this is the case, loss of astrocytic NL2 more broadly should enhance inhibitory synaptogenesis. Alternatively, the increase in the frequency of mIPSCs might be due to changes in the presynaptic release properties of inhibitory synapses. Together, these findings reveal a critical and previously unknown role for astrocytic NL2 as an essential governor of excitatory and inhibitory synaptic function in the cortex.

We have uncovered several unknown cell biological aspects of astrocyte–neuron interactions that control the development of cortical astrocytes, and have shown that astrocytic neuroligins have a crucial role in synaptogenesis. Bidirectional signalling via the astrocytic neuroligin and neuronal neurexin adhesions might directly regulate synapse formation and function. Alternatively, astrocytic neuroligins might control

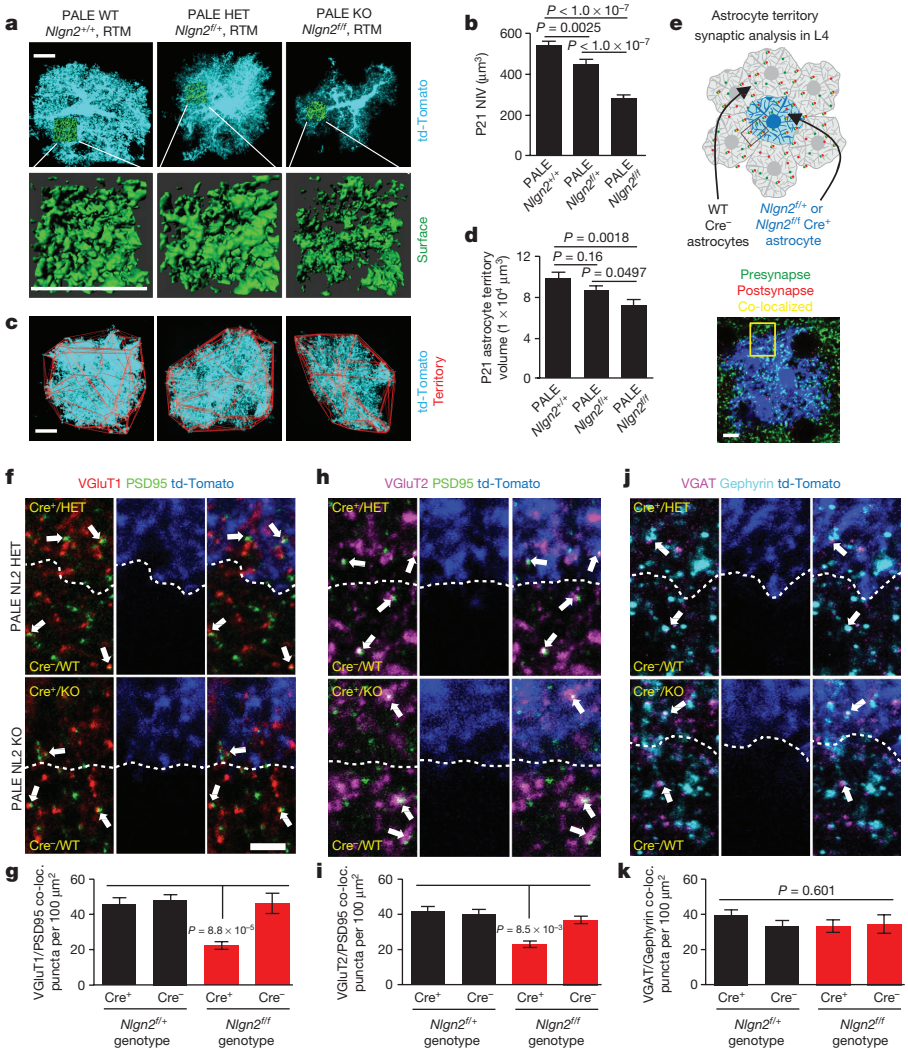

Figure 4 | Astrocytic NL2 controls astrocyte morphogenesis and excitatory synapse numbers. a, Images of V1 L4 PALE astrocytes (cyan) and NIVs (green) from the P21 *Nlgn2*$^{+/+}$, *Nlgn2*$^{f/+}$, and *Nlgn2*$^{f/f}$ mice labelled with td-Tomato from the Cre-dependent RTM transgene. **b**, Average NIV of td-Tomato/Cre^{+} PALE astrocytes. Three NIVs per cell, 16–20 cells per condition, four mice per condition. **c**, Images of V1 L4 td-Tomato/Cre^{+} P21 PALE astrocytes (cyan) and their territories (red outlines). **d**, Average territory volumes of td-Tomato/Cre^{+} PALE astrocytes. Between 16 and 20 cells per condition, four mice per condition. **e**, Schematic of local synapse density analysis. Synapse numbers were quantified within regions of interest inside the territories of V1 L4 P21 td-Tomato/Cre^{+} astrocytes (blue) and neighbouring Cre^{-} astrocytes (not visible). **f**, **h**, **j**, Images of intracortical excitatory synapses (**f**, VGluT1 (red) and PSD95 (green)), thalamocortical excitatory synapses (**h**, VGluT2 (magenta) and PSD95 (green)), and inhibitory synapses (**j**, VGAT (magenta) and gephyrin (cyan)). Dotted lines show astrocyte territory boundaries and arrows mark co-localized synaptic puncta. **g**, **i**, **k**, Quantification of average intracortical (**g**), thalamocortical (**i**), and inhibitory (**k**) synaptic co-localized puncta within td-Tomato/Cre^{+} PALE and Cre^{-} astrocyte territories of *Nlgn2*$^{f/+}$ and *Nlgn2*$^{f/f}$ mice. One ROI per territory (Cre^{+} and Cre^{-}) per image, five images per cell, three cells per mouse, four mice per genotype. One-way ANOVA (**b**, **d**, **g**, **i**, **k**). Data are means ± s.e.m. Scale bars, 10 µm (**a**, **c**, **e**), 2 µm (**f**, **h**, **j**).

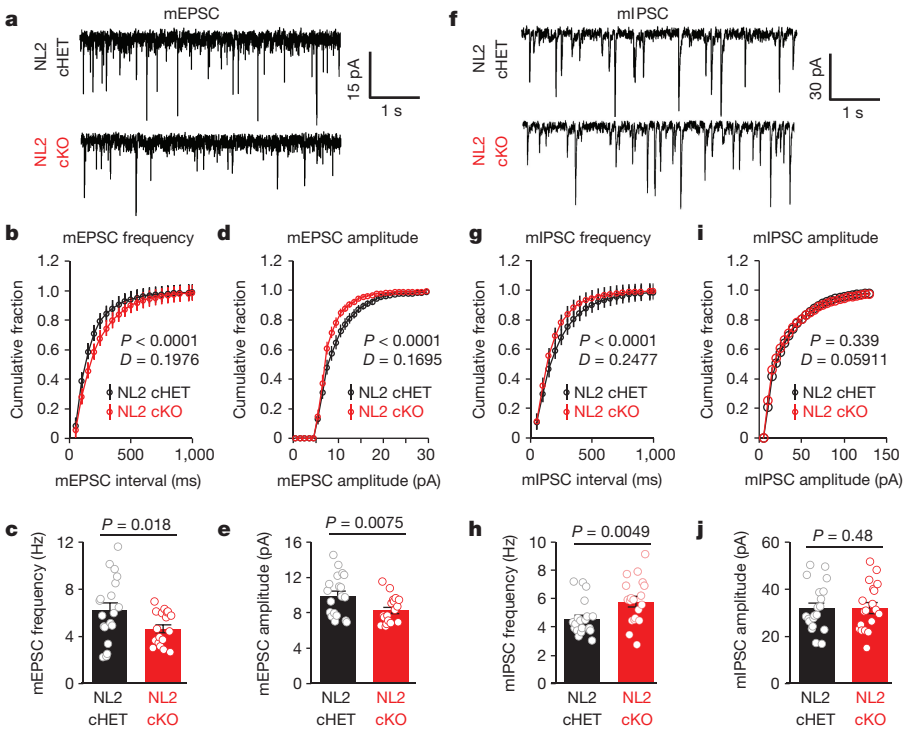

Figure 5 | Loss of NL2 in a large population of astrocytes alters excitatory and inhibitory synapse function. a, mEPSC traces from L5 pyramidal neurons in acute V1 slices of P21 NL2 cHET (black) and NL2 cKO (red) mice. **b**, **d**, Cumulative distributions of mEPSC frequency (**b**) and amplitude (**d**) from NL2 cHET and NL2 cKO pyramidal neurons. **c**, **e**, Average neuron mEPSC frequency (**c**) and amplitude (**e**) from NL2 cHET and NL2 cKO mice. **a**–**e**, Between 18 and 19 neurons per genotype. **f**, mIPSC traces from L5 pyramidal neurons in acute V1 slices of P21 NL2 cHET and NL2 cKO mice. **g**, **i**, Cumulative distributions of mIPSC frequency (**g**) and amplitude (**i**) from NL2 cHET and NL2 cKO L5 neurons. **h**, **j**, Average mIPSC frequency (**h**) and amplitude (**j**) from neurons of NL2 cHET and NL2 cKO mice. **f**–**j**, Between 19 and 20 neurons per genotype. Two sample Kolmogorov–Smirnov test (**b**, **d**, **g**, **i**), one-sided *t*-test (**c**, **e**, **h**, **j**). Data are means ± s.e.m.

synaptic connectivity by altering the expression and/or directed release of synaptogenic factors, such as thrombospondins, SPARCL1 (also known as Hevin) and glypicans[33–35], from astrocytes. Future studies exploring the link between neuroligin-mediated astrocyte–neuron adhesions and the regulation of astrocyte-induced synaptogenesis are necessary to test these possibilities.

Our findings also challenge the assumption that neuroligins are functional only within neurons in the brain. This is particularly important because gene mutations in neuroligins, including *NLGN2*, are associated with a number of neurological disorders such as autism and schizophrenia[36,37]. Neuroligin dysfunction in disease has been postulated to alter the fine balance between inhibition and excitation in the brain[38]. Here we demonstrate that astrocytic NL2 controls the balance of excitatory and inhibitory synaptic connectivity, indicating that synaptic pathologies associated with neuroligin mutations could originate from astrocytic dysfunction. A recent study found that glial progenitor cells from schizophrenic patients express significantly lower levels of NL1, NL2, and NL3 compared to controls. When these human glial progenitors were injected into mice, they caused neuronal dysfunction, perturbed animal behaviour and yielded abnormal astrocytic morphologies[39]. In conclusion, our findings reveal how imperative it is to understand the full extent of neuroligin functions in all cell types of the brain to completely comprehend the pathophysiology of these disorders.

Online Content Methods, along with any additional Extended Data display items and Source Data, are available in the online version of the paper; references unique to these sections appear only in the online paper.

Data Availability The data that support the findings of this study are included in the manuscript. Source Data are provided for Figs 1–5 and Extended Data Figs 1–10. Methods are provided within the Supplementary Information.

Received 10 April; accepted 17 October 2017.

1. Clarke, L. E. & Barres, B. A. Emerging roles of astrocytes in neural circuit development. *Nat. Rev. Neurosci.* **14,** 311–321 (2013).
2. Khakh, B. S. & Sofroniew, M. V. Diversity of astrocyte functions and phenotypes in neural circuits. *Nat. Neurosci.* **18,** 942–952 (2015).
3. Ma, Z., Stork, T., Bergles, D. E. & Freeman, M. R. Neuromodulators signal through astrocytes to alter neural circuit activity and behaviour. *Nature* **539,** 428–432 (2016).
4. Oberheim, N. A. *et al.* Uniquely hominid features of adult human astrocytes. *J. Neurosci.* **29,** 3276–3287 (2009).
5. Freeman, M. R. Specification and morphogenesis of astrocytes. *Science* **330,** 774–778 (2010).
6. Burda, J. E. & Sofroniew, M. V. Reactive gliosis and the multicellular response to CNS damage and disease. *Neuron* **81,** 229–248 (2014).
7. Stichel, C. C., Müller, C. M. & Zilles, K. Distribution of glial fibrillary acidic protein and vimentin immunoreactivity during rat visual cortex development. *J. Neurocytol.* **20,** 97–108 (1991).
8. Morel, L., Higashimori, H., Tolman, M. & Yang, Y. VGluT1+ neuronal glutamatergic signaling regulates postnatal developmental maturation of cortical protoplasmic astroglia. *J. Neurosci.* **34,** 10950–10962 (2014).
9. Cahoy, J. D. *et al.* A transcriptome database for astrocytes, neurons, and oligodendrocytes: a new resource for understanding brain development and function. *J. Neurosci.* **28,** 264–278 (2008).
10. Li, M. *et al.* Synaptogenesis in the developing mouse visual cortex. *Brain Res. Bull.* **81,** 107–113 (2010).
11. Akerman, C. J., Smyth, D. & Thompson, I. D. Visual experience before eye-opening and the development of the retinogeniculate pathway. *Neuron* **36,** 869–879 (2002).
12. Srinivasan, R. *et al.* New transgenic mouse lines for selectively targeting astrocytes and studying calcium signals in astrocyte processes in situ and *in vivo*. *Neuron* **92,** 1181–1195 (2016).
13. Zhang, Y. *et al.* An RNA-sequencing transcriptome and splicing database of glia, neurons, and vascular cells of the cerebral cortex. *J. Neurosci.* **34,** 11929–11947 (2014).
14. Zhang, Y. *et al.* Purification and characterization of progenitor and mature human astrocytes reveals transcriptional and functional differences with mouse. *Neuron* **89,** 37–53 (2016).
15. Bemben, M. A., Shipman, S. L., Nicoll, R. A. & Roche, K. W. The cellular and molecular landscape of neuroligins. *Trends Neurosci.* **38,** 496–505 (2015).
16. Baudouin, S. & Scheiffele, P. SnapShot: Neuroligin-neurexin complexes. *Cell* **141,** 908 (2010).
17. Craig, A. M. & Kang, Y. Neurexin-neuroligin signaling in synapse development. *Curr. Opin. Neurobiol.* **17,** 43–52 (2007).
18. Venkatesh, H. S. *et al.* Neuronal activity promotes glioma growth through neuroligin-3 secretion. *Cell* **161,** 803–816 (2015).
19. Samarelli, A. V. *et al.* Neuroligin 1 induces blood vessel maturation by cooperating with the α6 integrin. *J. Biol. Chem.* **289,** 19466–19476 (2014).
20. Proctor, D. T. *et al.* Axo-glial communication through neurexin-neuroligin signaling regulates myelination and oligodendrocyte differentiation. *Glia* (2015). 10.1002/glia.22875
21. Graf, E. R., Zhang, X., Jin, S. X., Linhoff, M. W. & Craig, A. M. Neurexins induce differentiation of GABA and glutamate postsynaptic specializations via neuroligins. *Cell* **119,** 1013–1026 (2004).
22. Murai, K. K., Nguyen, L. N., Irie, F., Yamaguchi, Y. & Pasquale, E. B. Control of hippocampal dendritic spine morphology through ephrin-A3/EphA4 signaling. *Nat. Neurosci.* **6,** 153–160 (2003).
23. Dean, C. *et al.* Neurexin mediates the assembly of presynaptic terminals. *Nat. Neurosci.* **6,** 708–716 (2003).
24. Gokce, O. & Südhof, T. C. Membrane-tethered monomeric neurexin LNS-domain triggers synapse formation. *J. Neurosci.* **33,** 14617–14628 (2013).
25. Liang, J. *et al.* Conditional neuroligin-2 knockout in adult medial prefrontal cortex links chronic changes in synaptic inhibition to cognitive impairments. *Mol. Psychiatry* **20,** 850–859 (2015).
26. Madisen, L. *et al.* A robust and high-throughput Cre reporting and characterization system for the whole mouse brain. *Nat. Neurosci.* **13,** 133–140 (2010).
27. Baldwin, K. T. & Eroglu, C. Molecular mechanisms of astrocyte-induced synaptogenesis. *Curr. Opin. Neurobiol.* **45,** 113–120 (2017).
28. Poulopoulos, A. *et al.* Neuroligin 2 drives postsynaptic assembly at perisomatic inhibitory synapses through gephyrin and collybistin. *Neuron* **63,** 628–642 (2009).
29. Varoqueaux, F. *et al.* Neuroligins determine synapse maturation and function. *Neuron* **51,** 741–754 (2006).
30. Wang, Y. *et al.* Norrin/Frizzled4 signaling in retinal vascular development and blood brain barrier plasticity. *Cell* **151,** 1332–1344 (2012).
31. Liddelow, S. A. *et al.* Neurotoxic reactive astrocytes are induced by activated microglia. *Nature* **541,** 481–487 (2017).
32. Harris, K. D. & Shepherd, G. M. The neocortical circuit: themes and variations. *Nat. Neurosci.* **18,** 170–181 (2015).
33. Allen, N. J. *et al.* Astrocyte glypicans 4 and 6 promote formation of excitatory synapses via GluA1 AMPA receptors. *Nature* **486,** 410–414 (2012).
34. Christopherson, K. S. *et al.* Thrombospondins are astrocyte-secreted proteins that promote CNS synaptogenesis. *Cell* **120,** 421–433 (2005).
35. Kucukdereli, H. *et al.* Control of excitatory CNS synaptogenesis by astrocyte-secreted proteins Hevin and SPARC. *Proc. Natl Acad. Sci. USA* **108,** E440–E449 (2011).
36. Singh, S. K. & Eroglu, C. Neuroligins provide molecular links between syndromic and nonsyndromic autism. *Sci. Signal.* **6,** re4 (2013).
37. Sun, C. *et al.* Identification and functional characterization of rare mutations of the neuroligin-2 gene (NLGN2) associated with schizophrenia. *Hum. Mol. Genet.* **20,** 3042–3051 (2011).
38. Gao, R. & Penzes, P. Common mechanisms of excitatory and inhibitory imbalance in schizophrenia and autism spectrum disorders. *Curr. Mol. Med.* **15,** 146–167 (2015).
39. Windrem, M. S. *et al.* Human iPSC glial mouse chimeras reveal glial contributions to schizophrenia. *Cell Stem Cell* **21,** 195–208 (2017).

Supplementary Information is available in the online version of the paper.

Acknowledgements This work was supported by grants from the National Institutes of Health (RO1 DA031833 to C.E., RO1 DE022743 to R.-R.J., F31 NS092419 to J.A.S.) and a Holland Trice Brain Research Award to C.E. K.T.B. was supported by Foerster-Bernstein Family and the Hartwell Foundation. We thank the NHLBI light microscopy core for STED imaging. We thank N. Allen, M. Bagnat, D. Silver and S. Soderling for critical reading of the manuscript.

Author Contributions J.A.S. and C.E. designed the experiments and wrote the paper. All authors reviewed and edited the manuscript. J.A.S. performed experiments and analysed data. J.A.S. and J.R. performed immunohistochemistry and cell/synapse count analysis. R.-R.J. designed and D.L. and Y.-H.K. performed and analysed the electrophysiology experiments. J.A.S. and K.T.B. performed western blot analysis. J.A.S., E.E., and T.E. performed *in vitro* experiments and analysis.

Author Information Reprints and permissions information is available at www.nature.com/reprints. The authors declare no competing financial interests. Readers are welcome to comment on the online version of the paper. Publisher's note: Springer Nature remains neutral with regard to jurisdictional claims in published maps and institutional affiliations. Correspondence and requests for materials should be addressed to C.E. (cagla.eroglu@dm.duke.du).

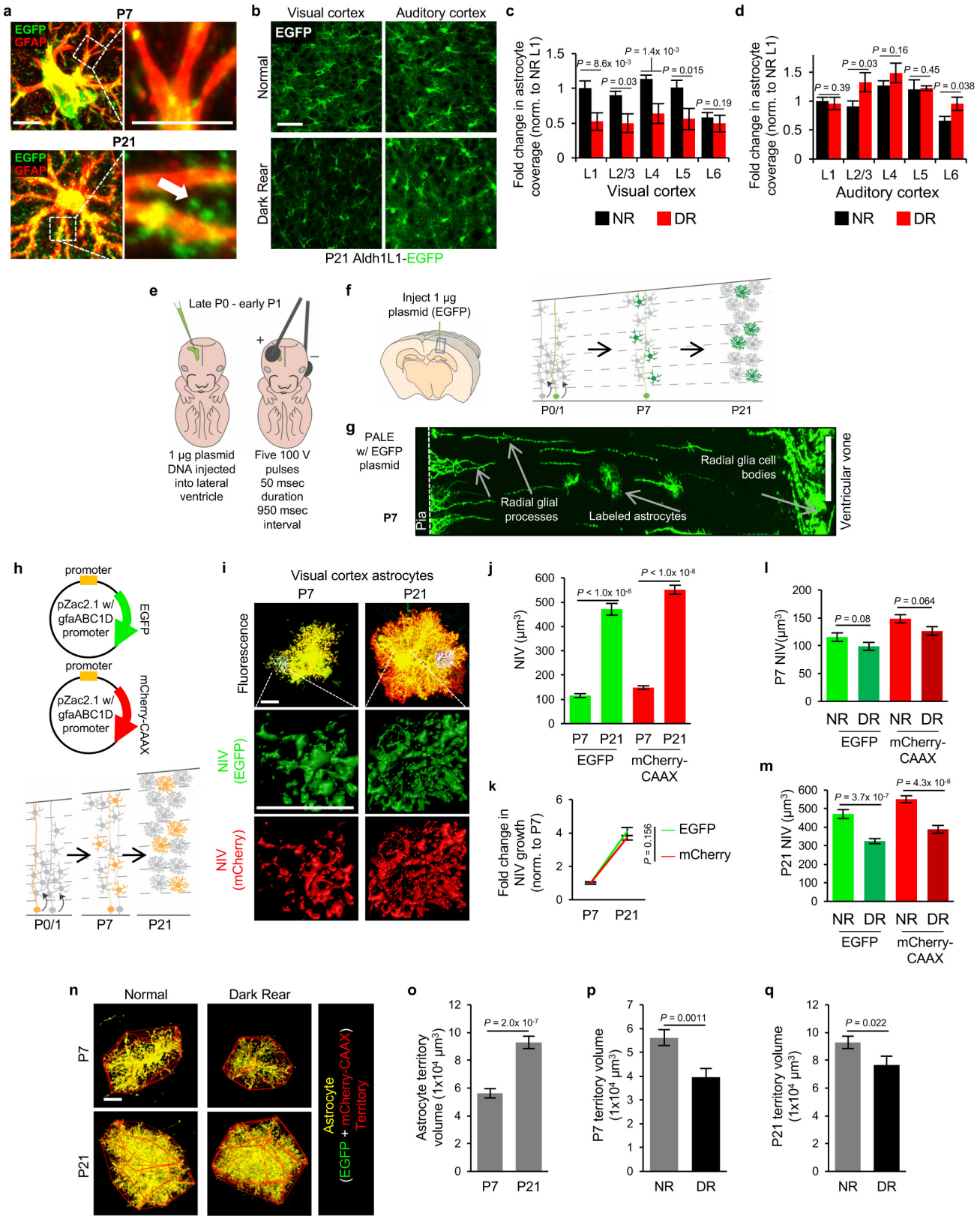

Extended Data Figure 1 | See next page for caption.

Extended Data Figure 1 | Astrocyte morphology is developmentally regulated in V1 cortex and occurs in parallel with sensory activity. **a**–**d**, Dark rearing reduces astrocyte morphogenesis in V1 visual cortex. **a**, High-magnification images of V1 L1 astrocytes from Aldh1L1–EGFP mice labelled with EGFP and GFAP at P7 and P21. Finer EGFP-labelled processes, which emerge by P21, do not stain with GFAP (arrow). **b**, Representative single optical section confocal images of V1 visual cortex (left) and A1 auditory cortex (right) L4 astrocytes from normal reared (NR, top) and dark reared (DR, bottom) Aldh1L1–EGFP mice at P21. **c**, Fold change in astrocyte coverage of the neuropil in normal and dark-reared mice at each layer of V1 cortex normalized to normal L1. $n = 10$ ROIs per layer, 3 images per mouse, 4 mice per condition. **d**, Fold change in astrocyte coverage of the neuropil in normal and dark-reared mice at each layer of A1 cortex normalized to normal L1. $n = 10$ ROIs per layer, 3 images per mouse, 4 mice per condition. **e**–**g**, Postnatal astrocyte labelling by electroporation (PALE) effectively transfects L4–5 astrocytes with plasmid DNA. **e**, Schematic of PALE in newborn mice. Late P0 or early P1 mouse pups are sedated by hypothermia and injected with 1 μg plasmid DNA into the lateral ventricle of one hemisphere with a pulled glass pipette. The plasmid solutions are mixed with a small volume of fast green dye for visualizing injections. Plasmids used in this study for PALE encoded EGFP, membrane-targeted mCherry (mCherry–CAAX), shRNAs also encoding EGFP, HA-tagged NL-related constructs, or Cre recombinase. Five pulses of 100 V are applied to the mouse head, using tweezer-trodes with the positive terminal situated above one hemisphere of V1 cortex. Please see Supplementary Methods for details. **f**, Diagram of PALE injection site and cartoon of V1 cortical development following PALE. Electroporation of plasmids at P0–P1 transfects the radial glial stem cells (light green), which give rise to astrocytes and other glia. At P7, labelled radial glial remnants persist and sparsely labelled developing astrocytes (dark green) are present predominantly in the lower cortical layers, L4–5. Two weeks later, radial glial remnants disappear and labelled mature astrocytes (dark green) are present. **g**, Representative tile scan image of V1 cortex at P7 following PALE with shCtrl plasmid. Radial glial cell bodies are visible near the ventricular surface. The labelled radial glia extend basal processes dorsally where they branch to form multiple endfeet associated with the pia (dotted line). Labelled astrocytes are dispersed throughout L4-5 of V1 cortex. These labelled astrocytes are imaged by high magnification confocal microscopy for more detailed volumetric analysis. **h**–**q**, Dark rearing reduces astrocyte morphogenesis at the single-cell level in V1. **h**, Schematic of PALE to test soluble and membrane-targeted fluorophores in astrocyte neuropil infiltration measurements. pZac2.1_gfaABC1D plasmid vectors expressing EGFP or membrane-targeted mCherry (mCherry–CAAX) reporters under the control of the minimal human GFAP promoter are co-electroporated into P0 wild-type D1 mice. Mice are housed in normal (NR) or dark rearing (DR) conditions, then killed at P7 or P21. **i**, Representative high-magnification confocal images and neuropil infiltration volume (NIV) reconstructions of PALE V1 cortex L4–5 astrocytes at P7 (left) and P21 (right). $EGFP^+$ (green) and $mCherry–CAAX^+$ (red) astrocytes (co-localized equals yellow) were uploaded to Imaris and the NIVs for each fluorophore were 3D reconstructed (middle and bottom). **j**, Average NIVs of V1 L4–5 PALE astrocytes at P7 and P21 for both EGFP and mCherry–CAAX fluorophores. Three NIVs per cell, 18–20 cells per condition, 4 mice per condition. **k**, Fold change in NIV growth curves from P7 to P21 astrocytes of EGFP and mCherry–CAAX fluorophores, normalized to P7 for each fluorophore. Three NIVs per cell, 18–20 cells per condition, 4 mice per condition. As expected, the membrane-bound fluorescent protein mCherry–CAAX slightly but significantly increased the visualization of astrocyte infiltration into the neuropil (mCherry–CAAX:EGFP; $P7 = 1.28 \pm 0.07$-fold, $P = 0.001$; $P21 = 1.17 \pm 0.04$-fold, $P = 0.005$). **l**, Average NIV of P7 astrocytes from normal and dark-reared mice using EGFP and mCherry–CAAX fluorophores. Three NIVs per cell, 18–20 cells per condition, 4 mice per condition. **m**, Average NIV of P21 astrocytes from normal and dark-reared mice using EGFP and mCherry–CAAX fluorophores. Three NIVs per cell, 18–20 cells per condition, 4 mice per condition. **n**, Representative high-magnification confocal images and territory reconstructions of V1 P7 and P21 PALE astrocytes from normal and dark-reared mice. The EGFP and mCherry–CAAX fluorophores (pseudo-coloured yellow) were used to reconstruct the astrocyte territory (red, see Supplementary Methods for further details). **o**, Average astrocyte territory volumes of V1 L4–5 PALE astrocytes at P7 and P21. Between 18 and 20 cells per condition, 4 mice per condition. **p**, Average territory volumes of V1 P7 PALE astrocytes from normal and dark-reared mice. Between 18 and 20 cells per condition, 4 mice per condition. **q**, Average territory volumes of V1 P21 PALE astrocytes from normal and dark-reared mice. Between 18 and 20 cells per condition, 4 mice per condition. One-sided *t*-test (**c**, **d**, **o**, **p**, **q**), one-way ANOVA (**j**, **l**, **m**), ANCOVA (**k**). Data are means ± s.e.m. Scale bars, 10 μm (**a**, **i**, **n**), 50 μm (**b**), 100 μm (**g**).

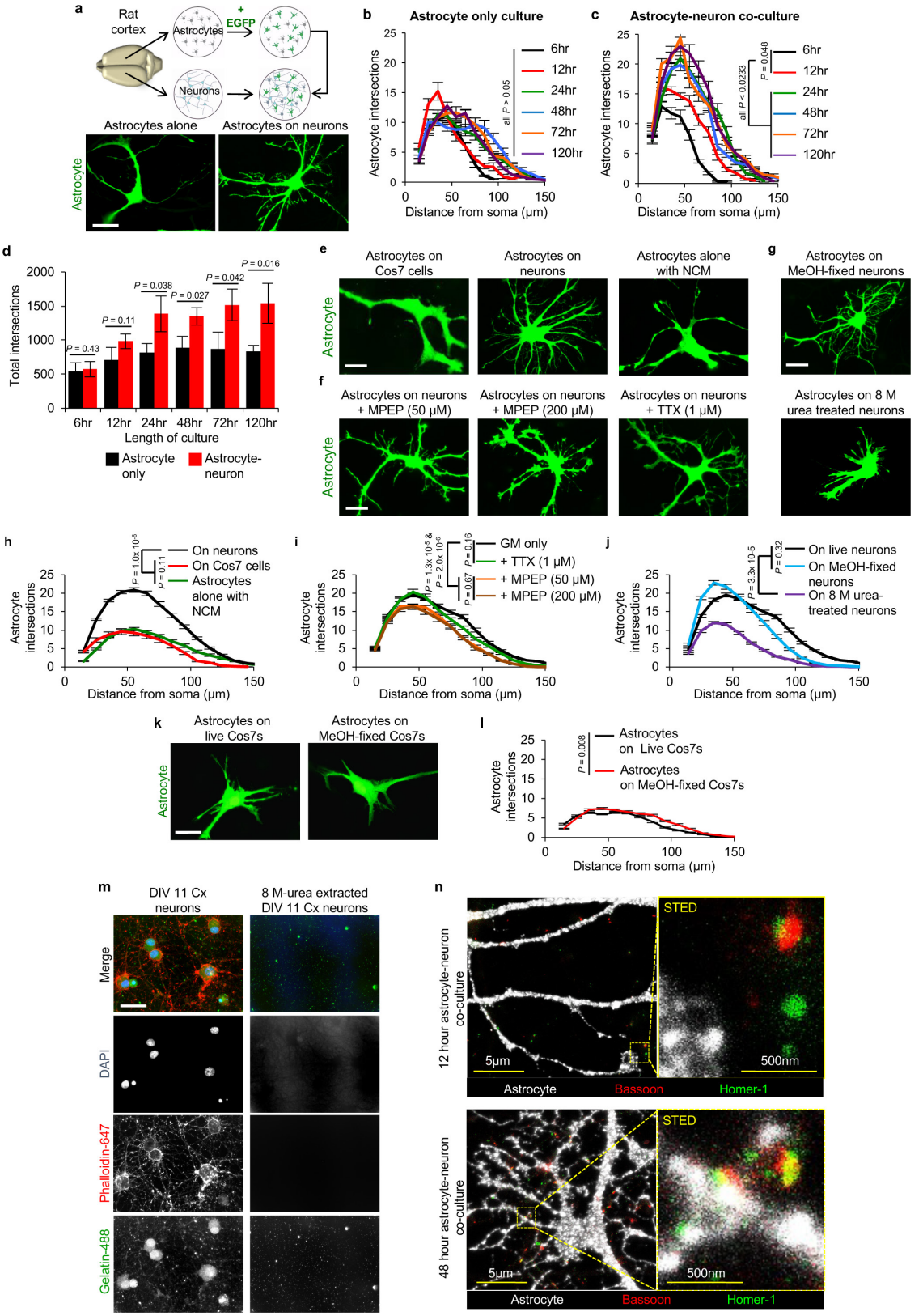

Extended Data Figure 2 | See next page for caption.

Extended Data Figure 2 | Direct neuronal contact controls astrocyte morphogenesis *in vitro*. **a**–**d**, Neurons induce astrocyte morphogenesis. **a**, Top, diagram of rat co-culture strategy used to test the cellular and molecular mechanisms of astrocyte–neuron interactions. Astrocytes and neurons are independently isolated from rat cortices (see Supplementary Methods for further details). Astrocytes are transfected after nine days *in vitro* (DIV9) with plasmid constructs (encoding EGFP, for example) and then trypsinized and plated onto cortical neurons at DIV11. Astrocytes and neurons are co-cultured for 48 h, unless otherwise indicated. Bottom, representative images of astrocytes alone or cultured with neurons (not shown). **b**, Sholl quantification of EGFP-transfected astrocyte morphology in astrocyte-only cultures at the indicated time points. The length of culture includes only the time of culture on PDL and laminin-coated coverslips (DIV11+), and not the isolation, purification, or transfection stages (DIV0–11, see Supplementary Methods). **c**, Sholl quantification of EGFP-transfected astrocyte morphology in co-culture with cortical neurons at the indicated time points. The length of culture includes only the time of co-culture with DIV11 rat cortical neurons and not the astrocyte isolation, purification, or transfection stages (DIV0–11). **d**, Quantification of total intersections obtained from Sholl analysis (**b**, **c**) of EGFP-transfected astrocytes grown alone (black) or on cortical neurons (red). **b**–**d**, Data represent one experiment with three biological replicates. Similar results were obtained in two independent experiments. $n > 15$ cells per condition per experiment. **e**–**n**, Direct contact of astrocytes with neurons or synapses regulates astrocyte morphogenesis *in vitro*. **e**, Representative images of EGFP-labelled astrocytes co-cultured with Cos7 cells, cortical neurons, or alone with neuron-conditioned medium (NCM). **f**, Representative images of EGFP-labelled astrocytes co-cultured with neurons in the presence of 50 μM or 200 μM MPEP or 1 μM TTX. **g**, Representative images of EGFP-labelled astrocytes plated on DIV11 methanol (MeOH)-fixed neurons or after neuronal processes were extracted with 8 M urea. **h**–**j**, Sholl quantification of astrocyte complexity under different culture conditions from **e**–**g**. Data represent one experiment with three biological replicates. Similar results were obtained in at least two independent experiments. $n > 25$ cells per condition per experiment. **k**, Representative images of EGFP-transfected astrocytes grown on live or MeOH-fixed Cos7 cells. **l**, Sholl quantification of EGFP-labelled astrocyte complexity from **k**. Data represent one experiment with three biological replicates. Similar results were obtained in two independent experiments. $n > 20$ cells per condition per experiment. **m**, Representative images of DIV11 cortical (Cx) neurons, processed normally or after neuronal processes were extracted with 8 M urea, stained for the following: DAPI (DNA, blue), phalloidin-conjugated 647 (filamentous actin/neuronal cell bodies and processes, red), gelatin-conjugated Oregon green 488 (ECM proteins, green). **n**, Representative stimulated emission depletion (STED) super-resolution micrographs of 12-h and 48-h astrocyte–neuron co-cultures immunostained for the pre- and postsynaptic markers Bassoon (red) and Homer-1 (green), respectively. Membrane-targeted EGFP-transfected astrocytes (pseudo-coloured white) extend lamellipodia-like structures towards synapses at the 12-h co-culture time point. By 48-h co-culture, astrocyte processes come in very close proximity to synaptic puncta demarcated by the co-localization of Bassoon and Homer-1. ANCOVA (**b**, **c**, **h**–**j**, **l**), one-tailed *t*-test (**d**). Data are means ± s.e.m. Scale bars, 10 μm (**a**, **e**, **f**, **g**, **k**, **m**), 5 μm and 500 nm (**n**).

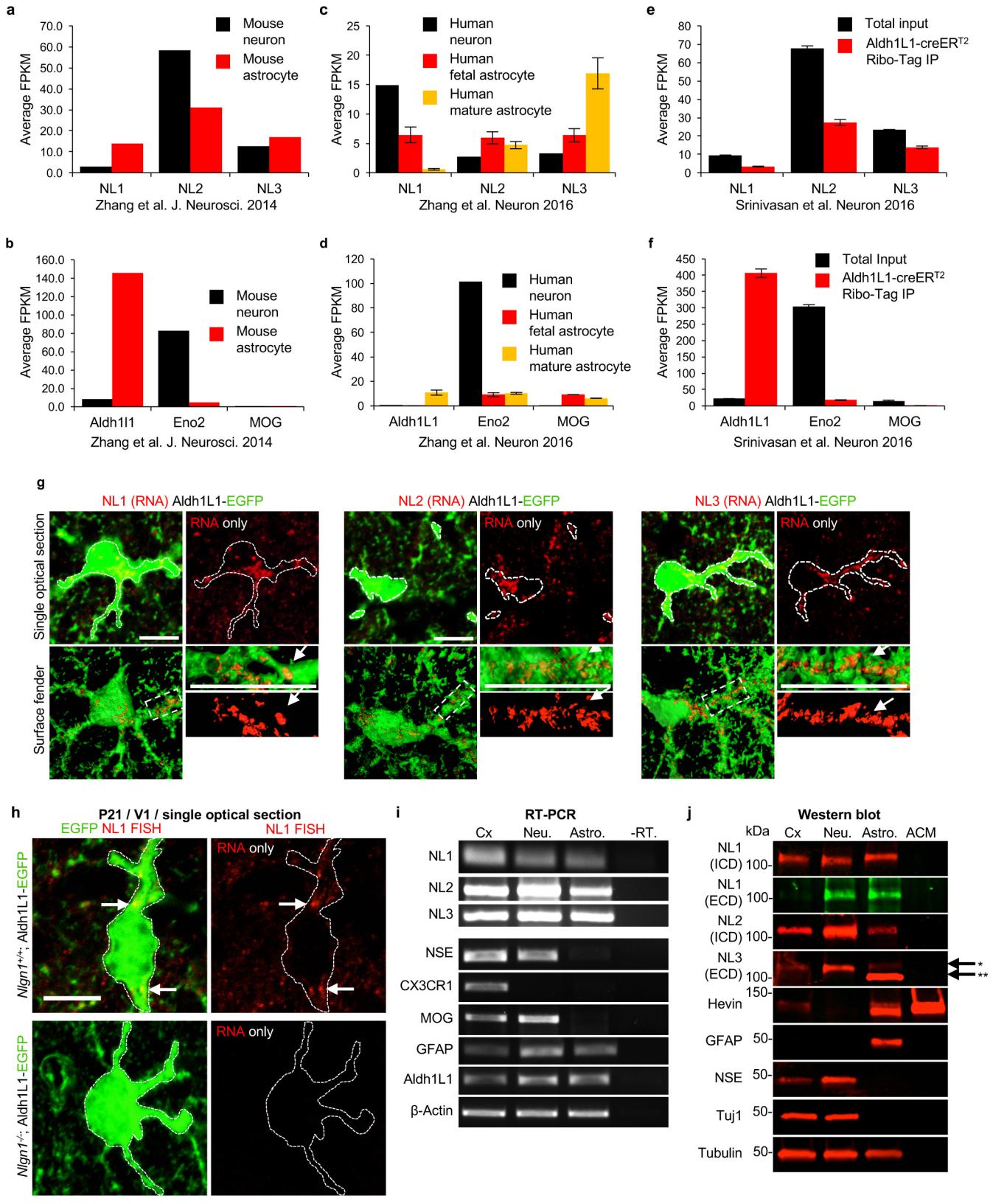

Extended Data Figure 3 | See next page for caption.

Extended Data Figure 3 | Neuroligins are expressed in astrocytes. **a**, Average fragments per kilobase of transcript per million reads (FPKM) of neuroligin mRNAs from RNA sequencing of P7 mouse neurons (black) and astrocytes (red; all data from ref. 13). **b**, Average FPKM values of cell-type specific transcripts from P7 neurons and astrocytes (Aldh1L1, astrocyte; Eno2, neuron; MOG, oligodendrocyte; all data from ref. 13). **c**, Average FPKM values of neuroligin mRNAs from 25-year-old human neurons (black), 18–18.5gw (gestational week) fetal astrocytes (red), and 8–63-year-old human mature astrocytes (yellow; all data from ref. 14). **d**, Average FPKM values of cell-type specific transcripts from specimens listed in **c** (all data from ref. 14). **e**, Average FPKM values of neuroligin mRNAs engaged with translating ribosomes from P80 mouse astrocytes (red) and total input (black) using Aldh1L1–creER^{T2}/Ribo-tag mice (all data from ref. 12). **f**, Average FPKM values of cell-type specific transcripts from specimens listed in **e** (all data from ref. 12). **g**, Single optical section confocal images (top) and 3D surface renderings (bottom) of FISH experiments with V1 L1 astrocytes (green) from P21 Aldh1L1–EGFP mice. NL1 (left, red), NL2 (middle, red), and NL3 (right, red) mRNAs are detected inside astrocyte somas and large branches (green, outlined). **h**, Representative images of RNA FISH experiments on NL1$^{+/+}$ (WT) and NL1$^{-/-}$ (KO) mice also containing the Aldh1L1–EGFP transgene labelling all astrocytes (green). NL1-specific RNA-FISH probes (red) were used to detect NL1 in both genetic backgrounds. Note: there is substantial fluorescence detection inside (dotted line, arrows) and outside NL1 wild-type astrocytes (top), but no detection of NL1 RNA-FISH signal in NL1 KO tissue sections (bottom). **i**, RT–PCR amplicons generated using transcript-specific exon-skipping primers. Lanes: P7 rat cortex (Cx), DIV11 rat cortical neuron cultures (Neu.), DIV11 rat cortical astrocyte cultures (Astro.), and DIV11 rat cortical astrocyte cultures without the reverse transcriptase enzyme to control for gDNA contamination (−RT). Specific primer sets were used to detect the following transcripts: NL1, NL2, NL3, neuron-specific enolase (NSE, neuron control), CX3C chemokine receptor 1 R1 (CX3CR1, microglia control), myelin oligodendrocyte glycoprotein (MOG, oligodendrocyte control), glial fibrillary acid protein (GFAP, astrocyte control), aldehyde dehydrogenase 1 family member 1 (Aldh1L1, astrocyte control), and β-actin (loading control). Astrocyte cultures do not contain detectible neuron, microglial or oligodendrocyte contamination. Cortical neuron cultures contain around 10% glial (astrocyte and oligodendrocyte) contamination. **j**, Western blot images. Lanes: P7 rat cortex (Cx), DIV11 rat cortical neuron cultures (Neu.), DIV11 rat cortical astrocyte cultures (Astro.), and rat cortical astrocyte-conditioned medium (ACM). Specific and validated antibodies were used to detect the following proteins: NL1 intracellular domain (NL1 ICD), NL1 extracellular domain (NL1 ECD), NL2 ICD, NL3 ECD, Hevin (astrocyte-specific secreted protein control), GFAP (intracellular astrocyte specific control), NSE (neuron control), Tuj1 (β3-tubulin, neuron control), tubulin (intracellular protein loading control). Note the presence of two bands for NL3 in the astrocyte sample. Single asterisks denote the expected full length protein. Astrocytes express a lower molecular weight NL3 (double asterisks) to a greater extent, but this lower molecular weight product is not present in the ACM, indicating that it is not a secreted NL3 species. For gel source data, see Supplementary Fig. 1. Data are means ± s.e.m. Scale bars, 10 μm.

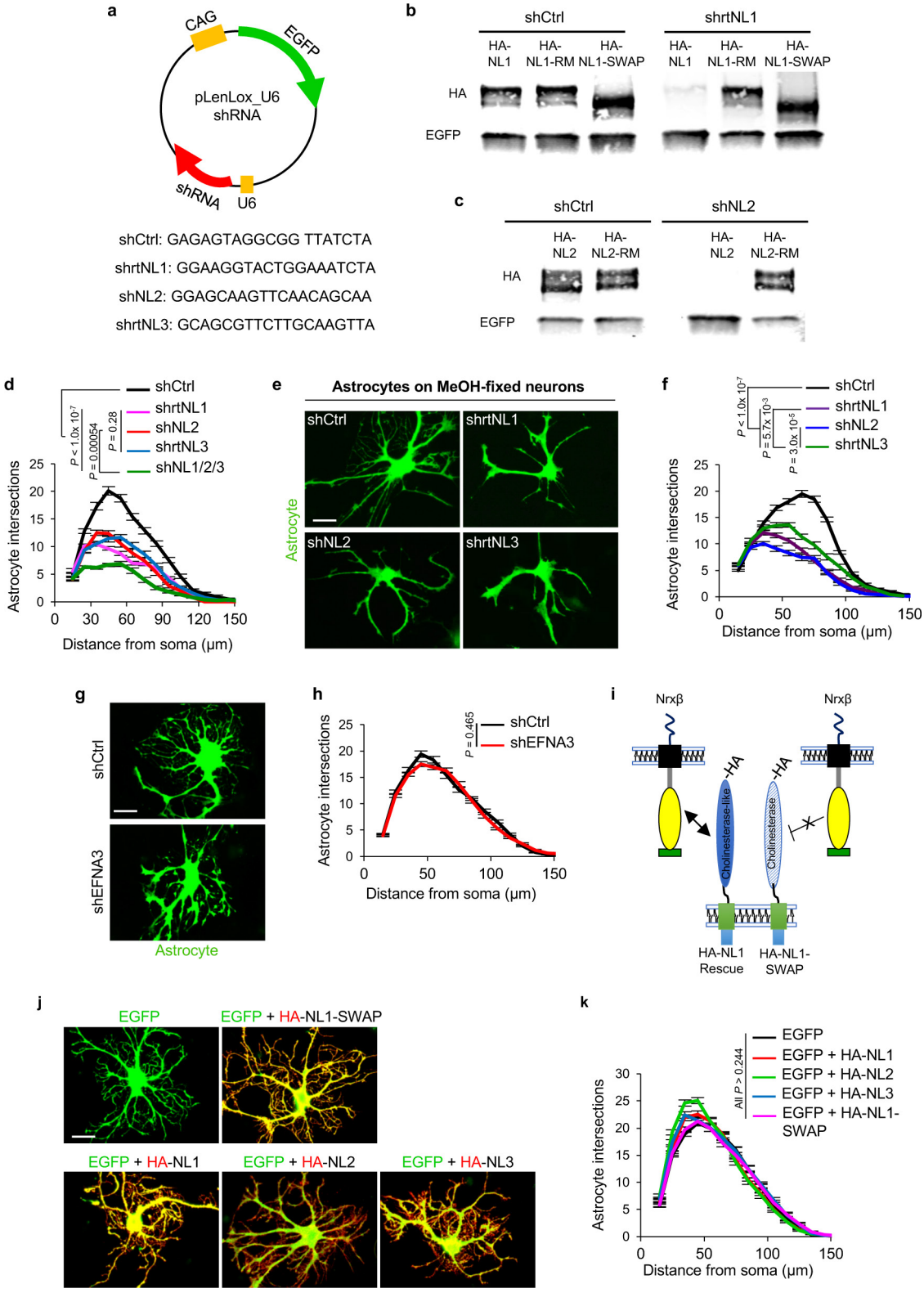

Extended Data Figure 4 | See next page for caption.

Extended Data Figure 4 | Neuroligin CAMs control neuron-induced astrocyte morphogenesis. a–**c**, Specificity of shRNAs against neuroligin sequences. **a**, Schematic representation of EGFP-expressing shRNA plasmids used to silence rat NLs *in vitro*. Sequences of shRNAs used on rat astrocytes against NL1, NL2, and NL3, as well as a scrambled shNL1 sequence used as a control (shCtrl). Rat-specific shRNAs against NL1, NL2, and NL3 were previously verified for efficiency and specificity[40,41]. The shNL2 sequence matches both rat and mouse NL2 sequences and effectively silences NL2 expression in cells from both species (Extended Data Fig. 6c, d). **b**, Western blot analyses of cell lysates from HEK293 cells transfected with shCtrl or shrtNL1 with various HA-tagged NL1 constructs. Full length NL1 (HA–NL1) is effectively silenced by shrtNL1, whereas the NL1 shRNA-resistant mutant (HA–NL1-RM) and NL1-SWAP are not silenced by shrtNL1. Note that NL1-SWAP runs smaller than full-length NL1 (previously published in ref. 23). **c**, Western blot analyses of cell lysates from HEK293 cells transfected with shCtrl or shNL2 with HA-tagged NL2 or HA-tagged NL2-RM. Full length NL2 (HA–NL2) is effectively silenced by shNL2, whereas NL2-RM is not. **b**, **c**, Antibodies against HA were used to detect the expression of neuroligins and the lysates were blotted for using an EGFP-specific antibody to verify transfection with shRNA plasmids. **d**-**k**, Neuroligins play significant roles in controlling neuron-induced astrocyte morphogenesis. **d**, Sholl quantification of astrocyte complexity of NL1, NL2, NL3, or NL1/2/3 silenced astrocytes cultured on cortical neurons (not visible, compare with Fig. 2a–e). Data represent one experiment with three biological replicates. Similar results were obtained in three independent experiments. $n > 25$ cells per condition per experiment. **e**, Representative images of shNL-transfected astrocytes (green) cultured with MeOH-fixed neurons (not visible). **f**, Sholl quantification of astrocyte complexity of neuroligin-silenced astrocytes cultured on MeOH-fixed neurons. Data represent one experiment with three biological replicates. Similar results were obtained in two independent experiments. $n > 20$ cells per condition per experiment. **g**, Representative images of transfected astrocytes (green) with shCtrl or an shRNA against EphrinA3 (EFNA3) in co-culture with neurons (not visible). EFNA3 is a CAM expressed in astrocytes that regulates astrocyte–synapse interactions in the hippocampus[22]. **h**, Sholl quantification of astrocyte complexity in shCtrl and shEFNA3-transfected astrocytes in co-culture with neurons. Data represent one experiment with three biological replicates. Similar results were obtained in two independent experiments. $n > 20$ cells per condition per experiment. **i**, Cartoon representation of NL1 domain structure. Neuroligins are type I transmembrane proteins with a large N-terminal extracellular domain (ECD). The NL1-ECD contains a cholinesterase (ChoE)-like domain that interacts with Nrxβs transcellularly. In NL1-SWAP, the ChoE-like domain is swapped for the ChoE sequence. This chimaera is efficiently trafficked to the cell surface, but fails to interact transcellularly with Nrxβs[23]. **j**, Representative images of astrocytes overexpressing EGFP (green) and HA-tagged neuroligins (red) in co-culture with neurons (not visible). Neuroligin-overexpressing astrocytes do not show any reductions in neuron-induced astrocyte morphogenesis. **k**, Sholl quantification of astrocyte complexity when overexpressing HA-tagged neuroligins. Data represent one experiment with three biological replicates. Similar results were obtained in two independent experiments. $n > 20$ cells per condition per experiment. ANCOVA (**d**, **f**, **h**, **k**). For gel source data, see Supplementary Fig. 1. Data are means ± s.e.m. Scale bars, 10 μm.

40. Chih, B., Gollan, L. & Scheiffele, P. Alternative splicing controls selective trans-synaptic interactions of the neuroligin–neurexin complex. *Neuron* **51,** 171–178 (2006).
41. Singh, S. K. *et al.* Astrocytes assemble thalamocortical synapses by bridging NRX1α and NL1 via Hevin. *Cell* **164,** 183–196 (2016).

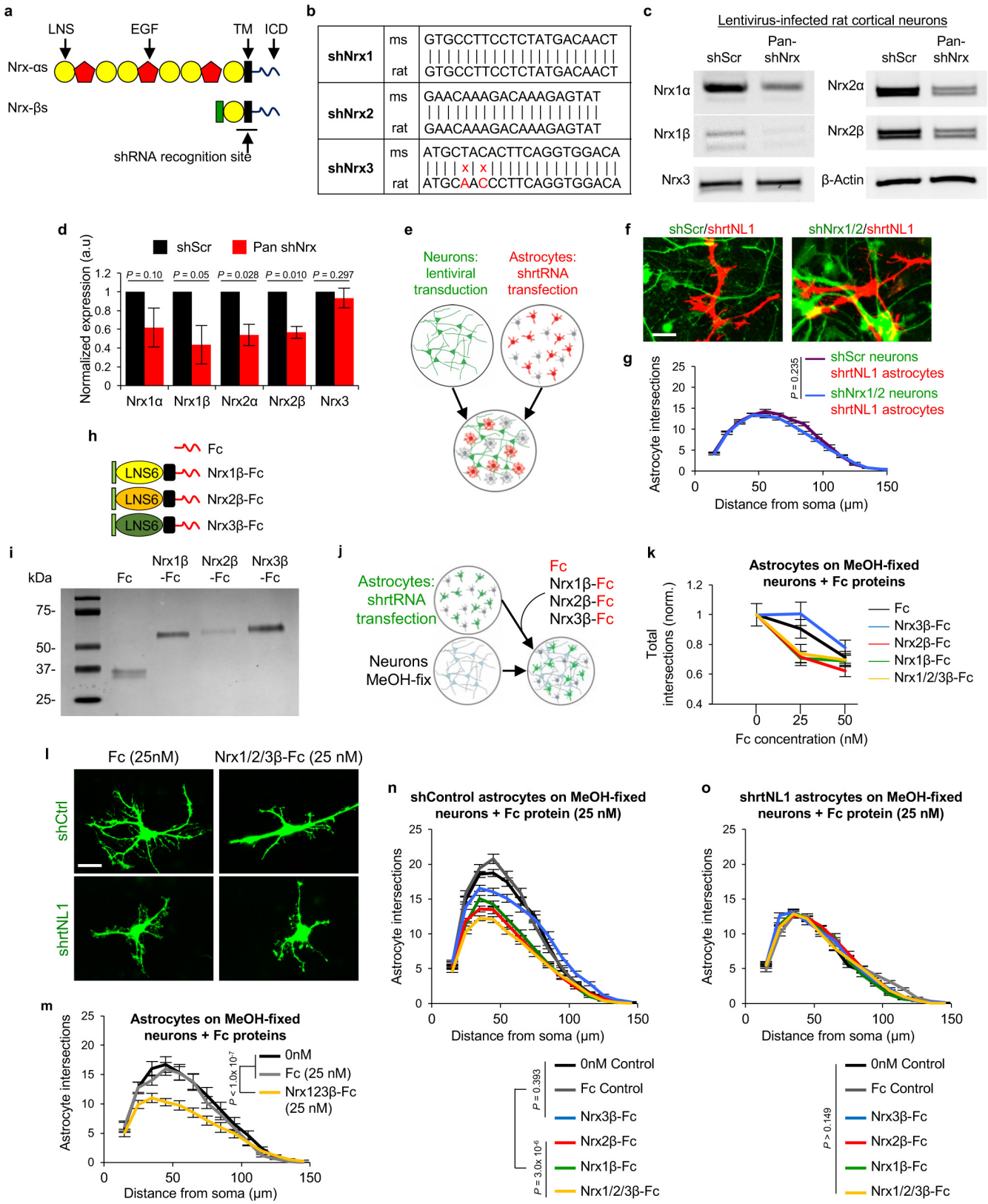

Extended Data Figure 5 | See next page for caption.

Extended Data Figure 5 | Astrocytic NL1 interacts with neuronal neurexins to promote astrocyte morphogenesis *in vitro*. **a**–**d**, Lentiviral knockdown of rat Nrx1 and Nrx2. **a**, Domain structures of Nrxα and Nrxβs. Nrxα and Nrxβs are expressed by alternative promoters and share the same LNS6 (laminin-α, neurexin and sex hormone-binding globulin 6), transmembrane and intracellular domains. Nrxαs contain five additional LNS domains and three EGF domains in their extracellular region. Gokce *et al.* generated a lentiviral construct with tandem shRNAs with recognition sequences localized to the LNS6 and TM domains of mouse Nrxs, such that both Nrxα and Nrxβs are silenced[24]. **b**, shRNA sequences that silence mouse Nrxα and Nrxβs[24] compared to the corresponding rat sequences. Based on sequence homology, we predicted that this lentiviral construct would silence rat Nrx1α/β and Nrx2α/β, but not Nrx3α/β owing to base-pair mismatches (red). **c**, RT–PCR amplicons from cortical neurons transduced with a scrambled control lentivirus (shScr) or pan-shNrx lentivirus. Specific primers against Nrx1α, Nrx1β, Nrx2α, Nrx2β, and Nrx3 were used to detect the presence and levels of Nrx transcripts. β-Actin was used as a control. As predicted, pan-shNrx[24] effectively diminished expression of rat Nrx1 and Nrx2 but not Nrx3. **d**, Quantification of Nrx cDNA levels from shScr or pan-shNrx-transduced cortical neurons. **c**, **d**, Results are from two independent experiments. **e**–**o**, Neuronal neurexins are required to promote astrocyte morphogenesis. **e**, Diagram of astrocyte–neuron co-culture strategy used to test the requirement for neuronal neurexins in regulating astrocyte complexity. Neurons are transduced on DIV2 with a lentivirus expressing EGFP and tandem shRNAs that silence rat Nrx1 and Nrx2 (green). Astrocytes are transfected with shRNA plasmids, which also encode mCherry, on DIV9 and then plated with neurons on DIV11 for 48 h. **f**, Representative images of shrtNL1 mCherry-transfected astrocytes (red) in co-culture with shNrx1/2 or shScr lentivirus-transduced neurons (green). **g**, Sholl quantification of astrocyte complexity in shrtNL1-transfected astrocytes in co-culture with shScr or shNrx1/2-transduced neurons. Data represent one experiment with three biological replicates. Similar results were obtained in two independent experiments. $n > 25$ cells per condition per experiment. **h**, Schematic of soluble Fc-tagged Nrxβ ectodomains. Recombinant Fc-only and Nrx1β–Fc proteins were previously described[40]. For this study, we generated recombinant constructs to express and purify Nrx2β–Fc and Nrx3β–Fc proteins (see Supplementary Methods). **i**, Coomassie staining shows the molecular mass and purity of the recombinant Fc-tagged proteins. Note that Nrx2β–Fc stains weakly with Coomassie dye, probably because it has fewer positively charged amino acids compared to Nrx1β–Fc and Nrx3β–Fc. **j**, Schematic of *in vitro* experiments testing the requirement for neurexin–neuroligin interactions in the control of astrocyte complexity. shRNA EGFP-transfected astrocytes are plated onto MeOH-fixed neurons in the presence or absence of soluble Fc-tagged Nrxβ-ectodomain proteins or control Fc protein. **k**, Quantification of complexity of astrocytes grown on MeOH-fixed neurons with or without Fc-tagged proteins added at various concentrations. Total Sholl intersections are plotted as a function of increasing Fc-tagged protein concentration (normalized to 0 nM). In this assay, Fc protein concentrations above 25 nM reduced astrocyte morphogenesis nonspecifically; thus, all experiments were conducted at 25 nM concentration. Data represent one experiment with three biological replicates. Similar results were obtained in two independent experiments. $n > 25$ cells per condition per experiment. **l**, Representative images of shCtrl or shrtNL1-transfected astrocytes (green) cultured with MeOH-fixed neurons (not visible) in the presence of 25 nM Fc (control) or 25 nM Nrx1β–Fc, Nrx2β–Fc and Nrx3β–Fc (8.3 nM concentration each, total of 25 nM). **m**, Sholl quantification of astrocytes cultured on MeOH-fixed neurons with or without recombinant Fc proteins (25 nM total concentration). Data represent one experiment with three biological replicates. Similar results were obtained in two independent experiments. $n > 25$ cells per condition per experiment. **n**, Sholl quantification of shCtrl-transfected astrocytes cultured on MeOH-fixed neurons supplemented with recombinant Fc proteins (25 nM total concentration). Data represent one experiment with three biological replicates. Similar results were obtained in two independent experiments. $n > 25$ cells per condition per experiment. **o**, Sholl quantification of shrtNL1-transfected astrocytes cultured on MeOH-fixed neurons supplemented with recombinant Fc proteins (25 nM total concentration). Data represent one experiment with three biological replicates. Similar results were obtained in two independent experiments. $n > 25$ cells per condition per experiment. One-tailed *t*-test (**d**), ANCOVA (**g**, **k**, **m**–**o**). For gel source data, see Supplementary Fig. 1. Data are means ± s.e.m. Scale bars, 10 μm.

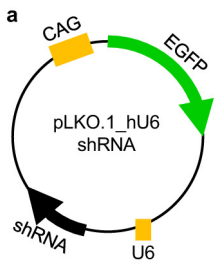

b

	shRNA sequence	Targets	Verification
shCtrl	GAGAGTAGGCGGTTATCTA		EDF. 6c-d
shNL1	CCCAACACTATACCAGGGATT	Mouse/Rat	EDF. 6c-d
shNL2	GAACAAAGACAAAGAGTAT	Mouse/Rat	EDF. 4c
shNL3	GCCCTTGGACTTAACATTTAT	Mouse/Rat	EDF. 6c-d

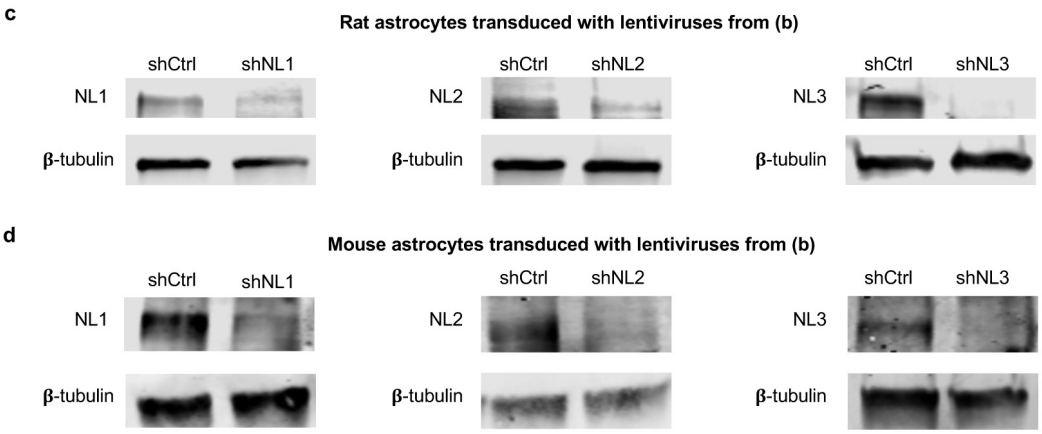

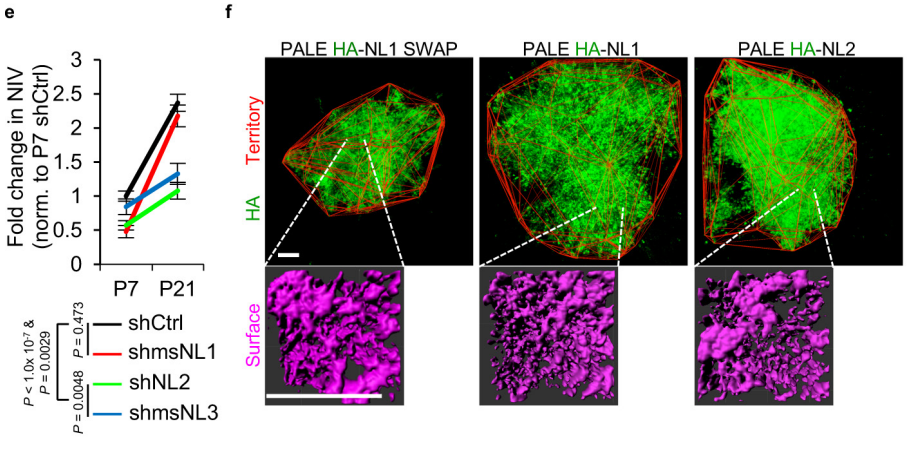

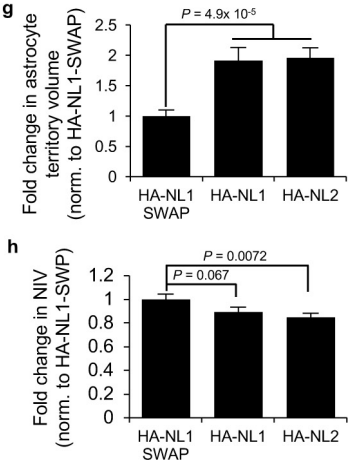

Extended Data Figure 6 | Astrocytic neuroligins control astrocyte morphogenesis *in vivo*. **a**–**d**, Verification of shRNAs used *in vivo*. **a**, Schematic of pLKO.1_hU6 plasmid vector housing the shRNA sequence and EGFP reporter. shRNA constructs targeting both mouse and rat NL1 and NL3 transcripts were obtained from Dharmacon. shNL2 used[40,41] effectively silences both mouse and rat NL2. In this plasmid backbone, the shRNA expression is driven from the human U6 minimal promoter. The commercially available plasmids do not encode a fluorescent protein reporter; therefore, we cloned EGFP under the control of a CAG promoter (see Supplementary Methods). **b**, shRNA sequences used to silence mouse neuroligins for PALE. Because they are a perfect match with the rat sequences, the same shRNAs also target rat neuroligins. shNL1 and shNL3 targeting vectors were verified here. shNL2 was verified previously[40,41] (and see Extended Data Fig. 4c). **c**, **d**, Western blot analysis of lysates from cultured rat (**c**) or mouse (**d**) astrocytes transduced with lentiviruses expressing shCtrl or shNLs. The shNLs effectively silenced the expression of endogenous NL1 (left), NL2 (middle) and NL3 (right) in both rat and mouse astrocytes. β-tubulin levels are shown as a loading control. Blots represent one experiment. Similar results were obtained from three separate experiments. **e**–**h**, Astrocytic neuroligins control astrocyte morphogenesis *in vivo*. **e**, Data from Fig. 3e, f normalized to P7 shCtrl astrocyte NIV values and replotted to determine how neuroligin silencing affects the growth trajectory of astrocyte NIV. shNL2 and shNL3-transfected astrocytes failed to expand their neuropil infiltration from P7 to P21, whereas shCtrl and shNL1-transfected astrocytes displayed robust (~2.5-fold) growth. Three NIV per cell, 10–20 cells per condition, at least three mice per condition. **f**, Top, representative images of P21 neuroligin-overexpressing PALE astrocytes from L4–5 V1 cortex. The territories of the neuroligin-overexpressing PALE astrocytes were determined in Imaris Bitplane software with a Matlab Xtension. This method identifies the terminal fluorescent points of each astrocyte and connects these points to generate the territory of each cell (red outline). Bottom, representative NIV (magenta) for neuroligin-overexpressing PALE astrocytes. **g**, Fold change in average territory volume of NL1- or NL2-overexpressing PALE astrocytes normalized to HA–NL1-SWAP. In the brains from three cohorts of seven PALE NL3-overexpressing mice, we were unable to find NL3-overexpressing astrocytes at P21, indicating that NL3-overexpression starting at P1 is not compatible with astrocyte survival and/or maturation. **h**, Fold change in average NIV of neuroligin-overexpressing PALE astrocytes normalized to HA–NL1-SWAP. Astrocytes might already occupy the available neuropil space; thus, neuroligin overexpression primarily forces astrocytes to expand. Alternatively, each neuroligin might direct astrocyte processes to certain neuronal elements; thus, neuroligin overexpression drives the astrocyte towards such structures, expanding their domains. **g**, **h**, Three NIVs per cell (**h** only), 14–20 cells per condition, 4 mice per condition. ANCOVA (**e**), one-way ANOVA (**g**, **h**). For gel source data, see Supplementary Fig. 1. Data are means ± s.e.m. Scale bars, 10 μm.

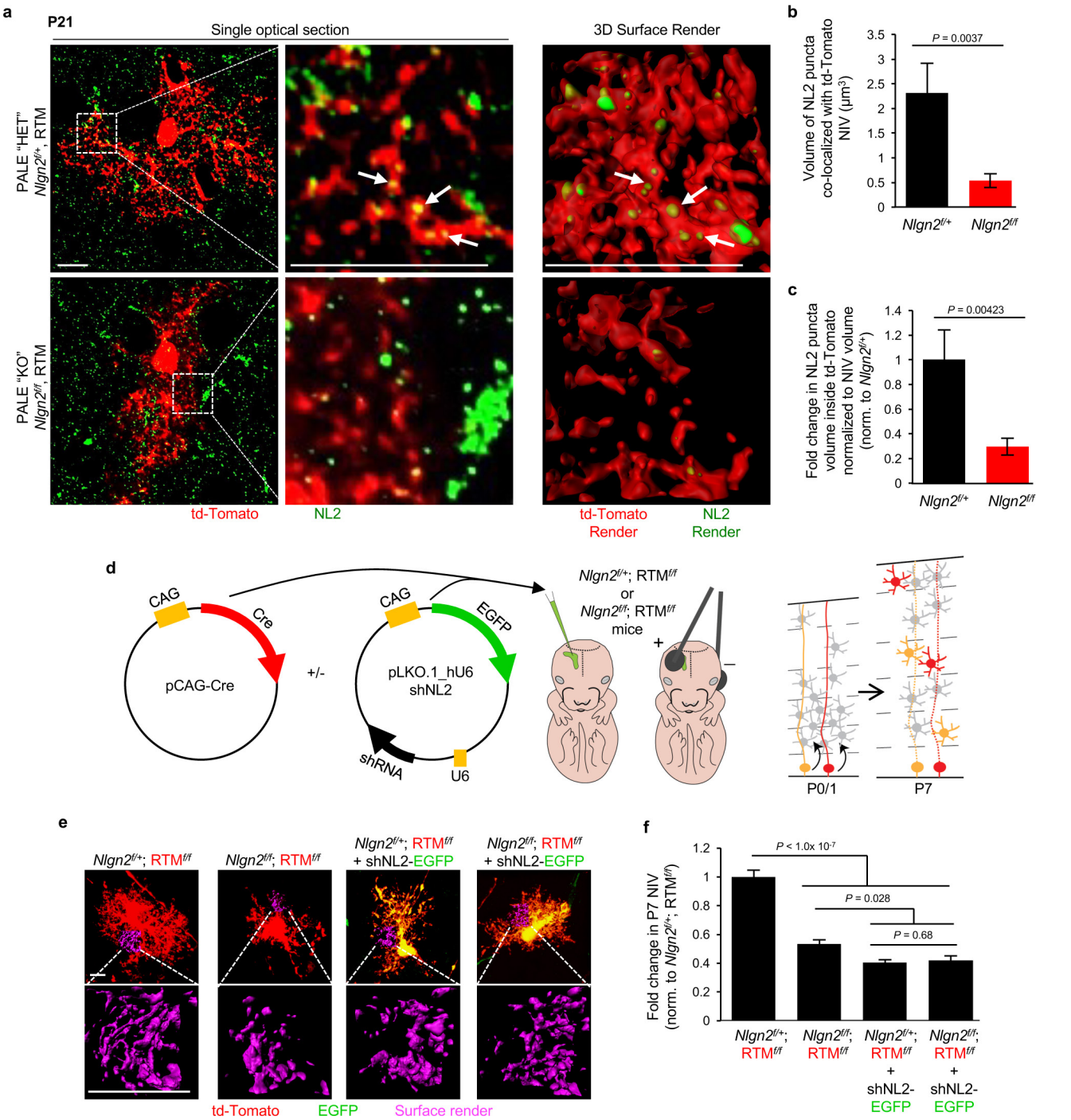

Extended Data Figure 7 | NL2 protein is expressed in astrocytes and is required for neuropil infiltration *in vivo*. **a**–**c**, NL2 protein staining in NL2 PALE HET and NL2 PALE KO astrocytes. **a**, Representative high-magnification Airyscan confocal images of P21 td-Tomato/Cre$^+$ PALE astrocytes from *Nlgn2*$^{f/+}$ and *Nlgn2*$^{f/f}$ (bottom) mice immunostained using an antibody against the intracellular domain of NL2. Left, single optical section of td-Tomato/Cre$^+$ astrocytes depicting NL2 staining (green) and td-Tomato/Cre$^+$ astrocyte (red). Middle, zoomed-in view of boxed region from left. Right, representative Imaris 3D reconstructed surface renderings of the co-localized NL2 (green) and td-Tomato/Cre$^+$ (red) signals in PALE NL2 HET and NL2 KO astrocytes (NL2 signal outside the td-Tomato/Cre$^+$ cell is not surface rendered). **b**, Quantification of average NL2 puncta volume inside td-Tomato/Cre$^+$ NIV of PALE NL2 HET and NL2 KO astrocytes. **c**, Fold change in NL2 puncta volume per td-Tomato/Cre$^+$ volume, normalized to NL2 HET. **b**, **c**, Two NIVs per image, three cells per mouse, three mice per genotype. **d**–**f**, shNL2 has no off-target effects in astrocytes *in vivo*. **d**, Approach to test the specificity of shNL2 *in vivo*. pCAG–Cre plasmid was injected with or without the shNL2 plasmid into P1 *Nlgn2*$^{f/+}$ or *Nlgn2*$^{f/f}$ pups that also contained two copies of the RTM reporter. Animals were killed at P7 for astrocyte morphological analysis. **e**, Representative images of P7 td-Tomato/Cre$^+$ astrocytes (red) or co-expressing shNL2 (green and red, appears as yellow) from PALE NL2 HET and NL2 KO mice. Representative NIVs are shown below each astrocyte (magenta). **f**, Fold change in average NIV of P7 td-Tomato/Cre$^+$ PALE NL2 HET and NL2 KO astrocytes with or without shNL2, normalized to td-Tomato/Cre$^+$ PALE NL2 HET. Three NIVs per cell, 16 cells per condition, at least 2 mice per genotype. One-tailed *t*-test (**b**, **c**), one-way ANOVA (**f**). Data are means ± s.e.m. Scale bars, 10 µm.

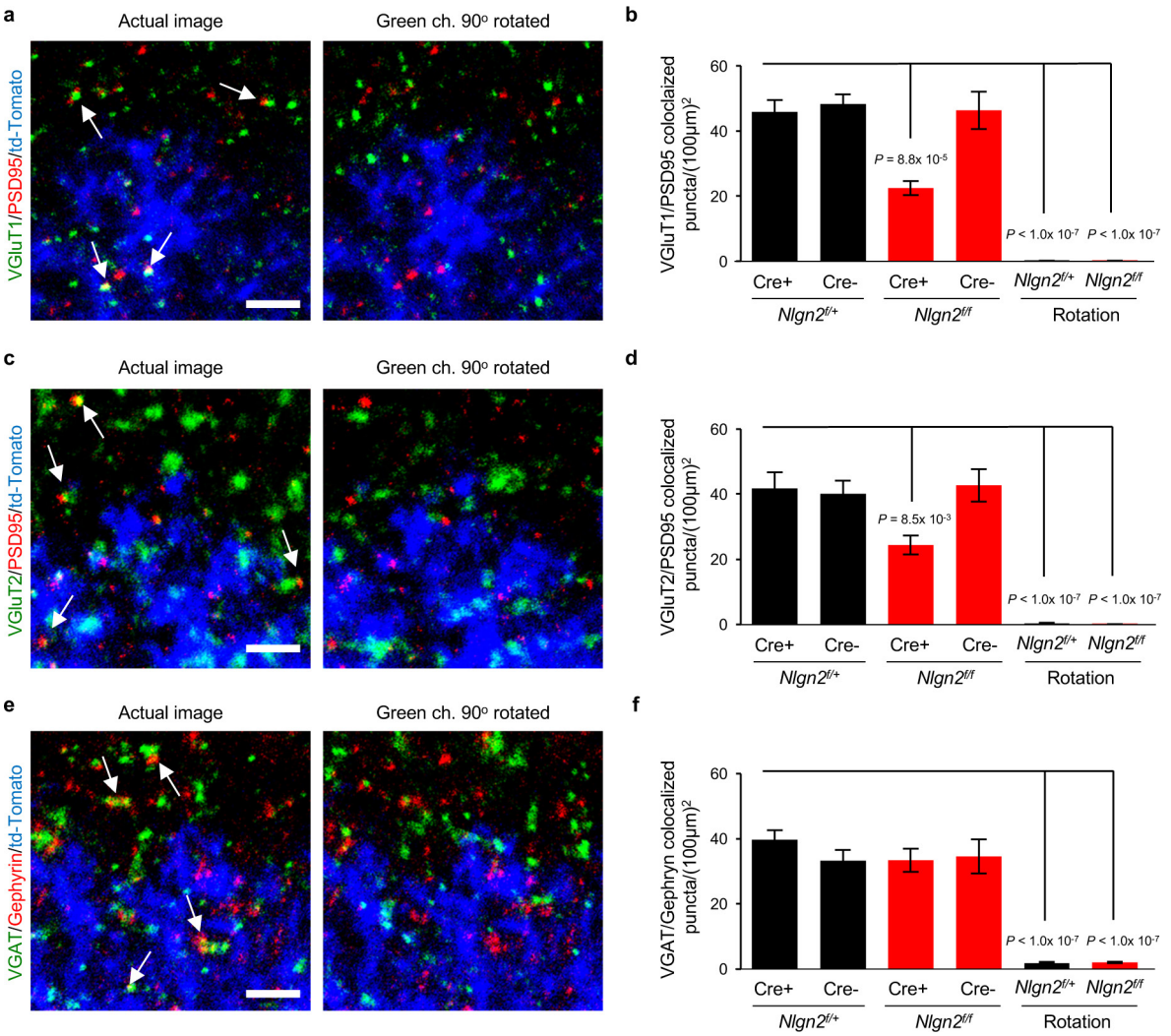

Extended Data Figure 8 | Controls determining the specificity of synaptic immunohistochemistry. a–f, To test whether synaptic immunostaining reflects true protein localization or random signal, a rotation analysis was performed[40]. In this test, the presynaptic channel was rotated 90° with respect to the other two channels and re-merged to create a rotated image. Synapse density quantifications were re-run using the rotated image compared to the standard image. **a**, **c**, **e**, Representative images of standard and rotated images stained for excitatory VGluT1 (red)/PSD95 (green) (**a**), excitatory VGluT2 (red)/PSD95 (green) (**c**), and inhibitory VGAT (red)/Gephyrin (green) (**e**) synaptic staining. Images depict the territory boundary of td-Tomato/Cre^{+} (blue) astrocytes and td-Tomato/Cre^{-} wild-type (unlabelled) astrocytes. **b**, **d**, **f**, Quantification of co-localized synaptic puncta density of standard and rotated images from excitatory VGluT1 (red)/PSD95 (green) (**a**), excitatory VGluT2 (red)/PSD95 (green) (**c**), and inhibitory VGAT (red)/Gephyrin (green) (**e**) synaptic staining. Standard images (left four bars) compared to the rotated images (right two bars). One-way ANOVA (**b**, **d**, **f**). Data are means ± s.e.m. Scale bar, 2 μm.

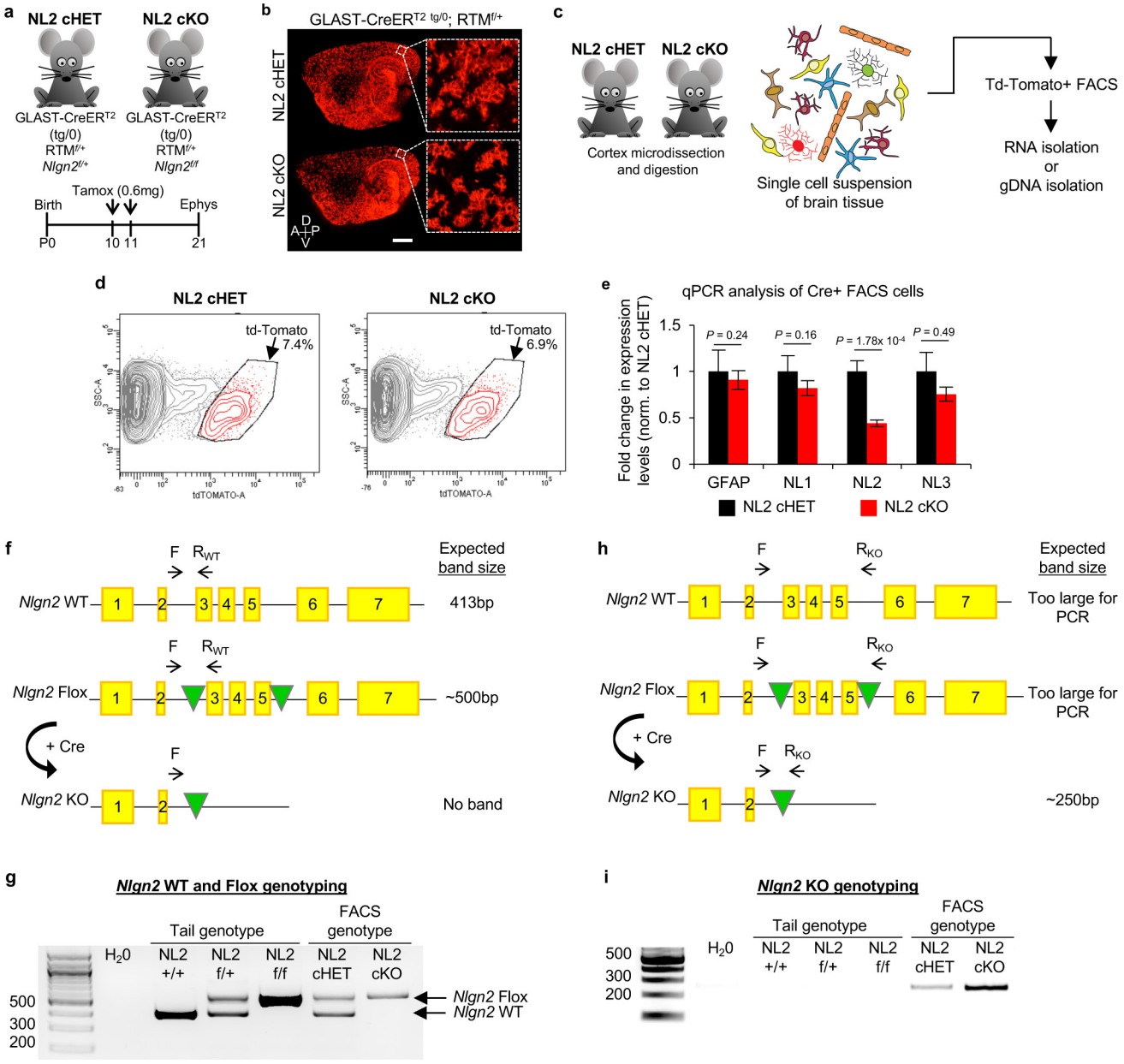

Extended Data Figure 9 | See next page for caption.

Extended Data Figure 9 | Generation and verification of NL2 conditional knockout mice. a, **b**, Generating astrocyte-specific conditional NL2 knockout mice using the tamoxifen-inducible GLAST-CreER^{T2} transgenic mouse line. **a**, Top, NL2 cHET and NL2 cKO mice each contain a single copy of the GLAST-CreER^{T2} transgene (tg/0) and the RTM reporter (*f*/+). (Bottom) Experimental timeline of tamoxifen-induced recombination of Cre-dependent loci (floxed *Nlgn2* and RTM) in combination with the GLAST-CreER^{T2} transgene. Cre recombination was activated by administering 0.6 mg tamoxifen twice at P10 and P11 via intraperitoneal injection to achieve widespread deletion of NL2 in astrocytes. **b**, Representative sagittal tile-scan confocal images of the forebrains of P21 NL2 cHET and NL2 cKO mice. td-Tomato/Cre^{+} cells (red) are visible in all regions of the forebrain. A higher magnification image of the V1 cortex is shown in the dotted box. More than 50% of cortical astrocytes in V1 are td-Tomato/Cre^{+} (see Extended Data Fig. 10 for quantification and details). A, P, D, V, are anterior, posterior, dorsal, ventral, respectively. **c**, **d**, Work-flow for isolating td-Tomato/Cre^{+} cells by FACS. **c**, Experimental flow chart demonstrating the isolation and analysis of td-Tomato/Cre^{+} cells from the cortices of NL2 cHET and NL2 cKO animals via FACS. Cortices were microdissected and papain digested, and a single-cell suspension was generated. The cell suspension was passed through a BD FACS sorter to sequester and capture td-Tomato/Cre^{+} cells. RNA was isolated from the td-Tomato^{+} cells, reverse transcribed to cDNA, then quantified by quantitative PCR. In separate experiments, genomic DNA (gDNA) was isolated from td-Tomato/Cre^{+} FACS samples to verify Cre-mediated recombination by PCR. **d**, Representative contour plots of NL2 cHET and cKO FACS analysis. Total single-cell suspension input was sorted and gated for td-Tomato fluorescence intensity (*x*-axis). The high td-Tomato^{+} cluster (red, boxed) was sorted into fresh tubes for RNA or gDNA extraction. **e**–**i**, Verification of the loss of NL2 in NL2 cKO astrocytes. **e**, qPCR quantification of gene transcript levels of GFAP, NL1, NL2 and NL3 in td-Tomato/Cre^{+} cells isolated by FACS from NL2 cHET (black) and cKO (red) mice. Expression is shown as fold change normalized to NL2 cHET values. Three or four mice per genotype. **f**, Schematic for genotyping the wild-type non-recombined alleles of NL2. The NL2 wild-type and floxed alleles have seven exons (labelled 1–7, yellow boxes). The NL2 floxed allele contains two LoxP sites (green triangles) that flank exons 3–5. To verify the non-Cre-mediated recombination of the NL2 locus by PCR, a reverse primer that base pairs with a region inside exon 3 is combined with a common forward primer that pairs with the DNA inside intron 2. The expected band sizes produced by the NL2 wild-type and floxed allele are 413 bp and about 500 bp, respectively. **g**, Representative non-recombined PCR gel with the following samples: water (control), tail samples from *Nlgn2*$^{+/+}$, *Nlgn2*$^{f/+}$, and *Nlgn2*$^{f/f}$ mice, and td-Tomato/Cre^{+} FACS samples from NL2 cHET and NL2 cKO brains. The wild-type and floxed alleles are depicted (arrows). **h**, Schematic for genotyping the knockout recombined alleles of NL2. To verify the Cre-mediated recombination of the NL2 locus by PCR, a reverse primer that base pairs with a region downstream of the second LoxP site inside intron 5 is combined with the common forward primer. The Cre-mediated recombined *Nlgn2* locus will produce a roughly 250-bp band. The non-recombined alleles (wild-type and non-recombined floxed alleles) will not produce a band small enough for detection. **i**, Representative Cre-mediated recombined PCR gel with the following samples: water (control), tail samples from *Nlgn2*$^{+/+}$, *Nlgn2*$^{f/+}$, and *Nlgn2*$^{f/f}$ mice, and td-Tomato^{+} FACS samples from NL2 cHET and NL2 cKO brains. For gel source data, see Supplementary Fig. 1. One-tailed *t*-test (**e**). Data are means ± s.e.m. Scale bar, 1 mm.

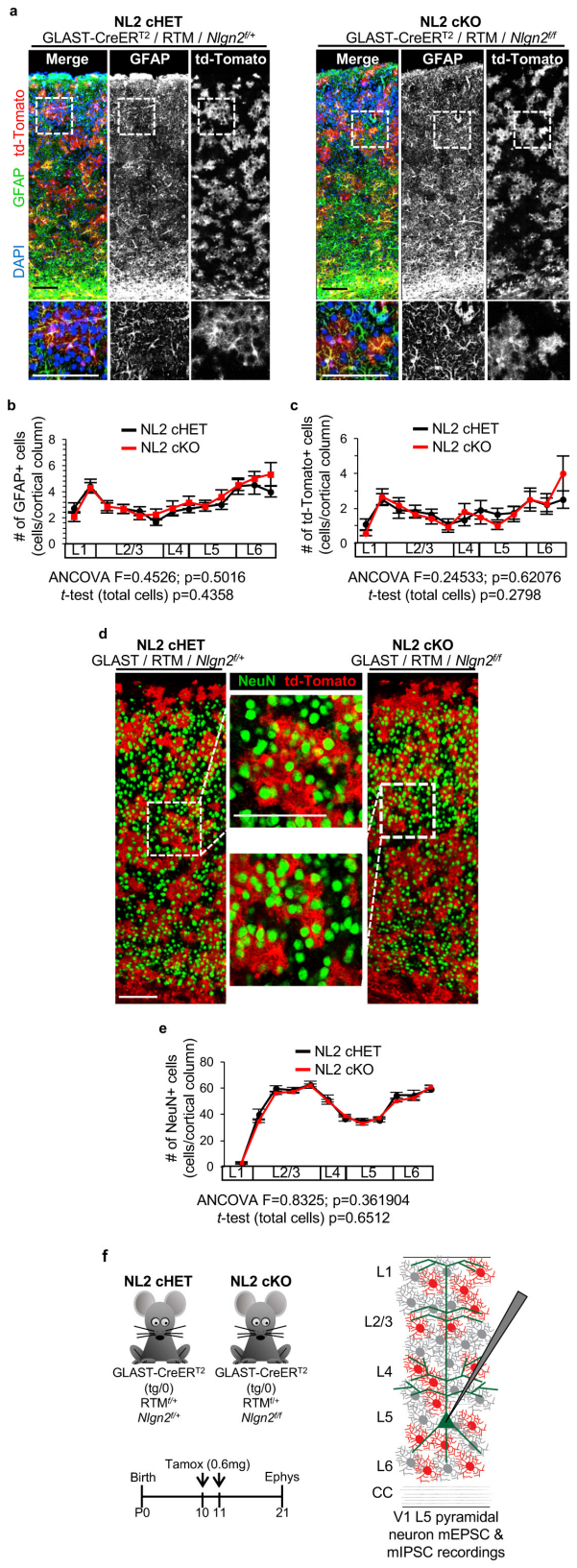

Extended Data Figure 10 | Conditional deletion of NL2 in astrocytes does not alter cell number or distribution. **a**–**c**, The number of astrocytes and td-Tomato/Cre^{+} cells are similar between NL2 cHET and NL2 cKO mice. **a**, Representative tile scan images of V1 cortex from NL2 cHET and NL2 cKO mice stained for GFAP (astrocyte marker, green), td-Tomato/Cre^{+} cells (red), and DAPI (blue). High magnification of selected regions is shown below each image (dotted box). More than 99% of td-Tomato/Cre^{+} cells stain positive for GFAP. **b**, Quantification of the number and distribution of V1 cortex GFAP^{+} astrocytes in NL2 cHET and NL2 cKO mice. The number of GFAP^{+} cells is plotted as a function of cortical layer (L1–6) in which they reside. The percentage of GFAP/td-Tomato double-positive cells in NL2 cHET and NL2 cKO mice does not differ significantly (NL2 cHET = 58.7 ± 4.0%; NL2 cKO = 53.9 ± 4.4%, $P = 0.31483$). Three or four images per mouse, three mice per genotype. **c**, Quantification of the number and distribution of td-Tomato/Cre^{+} cells from NL2 cHET and NL2 cKO mice in V1 cortex. The number of td-Tomato/Cre^{+} cells is plotted as a function of cortical layer. Three or four images per mouse, three mice per genotype. **d**, Representative tile scan images of V1 cortex from NL2 cHET and NL2 cKO mice stained for NeuN (neuronal marker, green) and td-Tomato/Cre^{+} cells (red). High magnification of selected regions is shown in dotted boxes. The percentage of NeuN/td-Tomato double-positive cells was extremely low, confirming that Cre recombination is specific to astrocytes in V1 cortex (number of NeuN/td-Tomato double-positive cells by genotype was: NL2 cHET, 36 double-positive cells out of 13,903 NeuN^{+} cells counted (0.26%); NL2 cKO, 36 double-positive cells out of 13,504 NeuN^{+} cells counted (0.25%). **e**, Quantification of the number and distribution of NeuN^{+} neurons from NL2 cHET and NL2 cKO mice. The number of NeuN^{+} cells is plotted as function of the cortical layer in which they reside. Three or four images per mouse, three mice per genotype. **f**, Top left, NL2 cHET and NL2 cKO mice used to test excitatory and inhibitory synaptic function. Bottom left, experimental timeline of tamoxifen-induced recombination of Cre-dependent loci (floxed *Nlgn2* and RTM) in combination with the GLAST-CreER^{T2} transgene. Cre was activated by administering 0.6 mg tamoxifen at P10 and P11 via intraperitoneal injection to achieve widespread deletion of NL2 in astrocytes. Right, schematic representation of electrophysiological recording experiments performed on L5 V1 pyramidal neurons from NL2 cHET and NL2 cKO mice. L5 pyramidal neurons receive excitatory and inhibitory synaptic connections from all cortical layers that contain td-Tomato/Cre^{+} (red) and td-Tomato/Cre^{-} (grey) astrocytes. mEPSCs and mIPSCs were recorded from L5 pyramidal neurons using acute slices from P21 NL2 cHET and NL2 cKO mice containing the V1 cortex. ANCOVA (**b**, **c**, **e**). Data are means ± s.e.m. Scale bars, 100 μm.

nature research

Corresponding author(s): Dr. Cagla Eroglu

☐ Initial submission ☒ Revised version ☐ Final submission

Life Sciences Reporting Summary

Nature Research wishes to improve the reproducibility of the work that we publish. This form is intended for publication with all accepted life science papers and provides structure for consistency and transparency in reporting. Every life science submission will use this form; some list items might not apply to an individual manuscript, but all fields must be completed for clarity.

For further information on the points included in this form, see Reporting Life Sciences Research. For further information on Nature Research policies, including our data availability policy, see Authors & Referees and the Editorial Policy Checklist.

Experimental design

1. Sample size

Describe how sample size was determined.

Sample size for each experiment is indicated in the figure legend for each experiment. The sample size was chosen based on previous experience for each experiment to yield high power to detect specific effects. No statistical methods were used to predetermine sample size.

2. Data exclusions

Describe any data exclusions.

No samples or analyses were excluded from in vitro experiments. Two animals were excluded from Extended Data Fig 9e based on identification of the lack of tamoxifen-induced allelic recombination to produce NL2KOs after the problem was traced back to a bad batch of tamoxifen. In sum their inclusion or exclusion does not alter the final conclusions of these analyses.

3. Replication

Describe whether the experimental findings were reliably reproduced.

All experimental findings were reliably reproducible.

4. Randomization

Describe how samples/organisms/participants were allocated into experimental groups.

For in vivo studies, animals were chosen based on correct genotypes, requiring 2 or 3 correct alleles. Specifically, animal pairs from the same litters were compared to decrease variance in age and rearing. However, each experiment contained animals from at least two different litters to ensure that the differences between genotypes can be observed in mice from different litters. Sex-specific differences were eliminated by including equal numbers of both sexes for all animal studies.

5. Blinding

Describe whether the investigators were blinded to group allocation during data collection and/or analysis.

For all in vitro experiments, the investigator performing the imaging and analyses was blind to the experimental conditions. For in vivo immunohistochemistry experiments, the investigator was blind to the experimental groups during the analyses. During the execution and analyses of the electrophysiological recordings, the electrophysiologist was blind to the genotypes of the individual animals.

Note: all studies involving animals and/or human research participants must disclose whether blinding and randomization were used.

6. Statistical parameters

For all figures and tables that use statistical methods, confirm that the following items are present in relevant figure legends (or in the Methods section if additional space is needed).

n/a	Confirmed
☐	☒ The exact sample size (*n*) for each experimental group/condition, given as a discrete number and unit of measurement (animals, litters, cultures, etc.)
☐	☒ A description of how samples were collected, noting whether measurements were taken from distinct samples or whether the same sample was measured repeatedly
☐	☒ A statement indicating how many times each experiment was replicated
☐	☒ The statistical test(s) used and whether they are one- or two-sided (note: only common tests should be described solely by name; more complex techniques should be described in the Methods section)
☐	☒ A description of any assumptions or corrections, such as an adjustment for multiple comparisons
☐	☒ The test results (e.g. *P* values) given as exact values whenever possible and with confidence intervals noted
☐	☒ A clear description of statistics including central tendency (e.g. median, mean) and variation (e.g. standard deviation, interquartile range)
☐	☒ Clearly defined error bars

See the web collection on statistics for biologists for further resources and guidance.

Software

Policy information about availability of computer code

7. Software

Describe the software used to analyze the data in this study.

Fluorescent imaging was acquired with Zen Software (Zeiss) or Leica Application Suite (LAS). Images were processed and analyzed using FIJI 2.0 (Sholl analysis), ImageJ Version 1.29 (synaptic puncta analysis by Puncta Analyzer Plugin, available by request -- cagla.eroglu@dm.duke.edu), Imaris 8.2.1 (Bitplane), and Matlab R2015b for Imaris plugins, ("Visualize Surface Spots" and "Convex Hull"). Statistica software (Statsoft) Version 7.1 was used for all statistical analyses, with the exception of the electrophysiological analysis, which was done with GraphPad Prism 6 and JMP (Pro13).

For manuscripts utilizing custom algorithms or software that are central to the paper but not yet described in the published literature, software must be made available to editors and reviewers upon request. We strongly encourage code deposition in a community repository (e.g. GitHub). *Nature Methods* guidance for providing algorithms and software for publication provides further information on this topic.

Materials and reagents

Policy information about availability of materials

8. Materials availability

Indicate whether there are restrictions on availability of unique materials or if these materials are only available for distribution by a for-profit company.

All materials are readily available from the authors or from standard commercial sources.

9. Antibodies

Describe the antibodies used and how they were validated for use in the system under study (i.e. assay and species).

Antibodies used for immunohistochemistry and/or western blotting:

Anti-human Alexa 594 - Life Technologies (A11014) - Immunostaining - rat cells; Validation: Manufacturer - https://www.thermofisher.com/antibody/product/Goat-anti-Human-IgG-H-L-Secondary-Antibody-Polyclonal/A-11014

Bassoon - Enzo (PS003F) - Immunostaining - rat cells, mouse tissues; Validation: Antibodypedia - https://www.antibodypedia.com/gene/13612/BSN/antibody/643844/ADI-VAM-PS003-F

Gephyrin - Synaptic Systems (147 021) - Immunostaining - mouse tissues; Validation: Manufacturer - https://www.sysy.com/products/gephyrin/facts-147021.php

GFAP - Dako (Z0334) - Immunostaining - mouse tissues; Validation:

GFAP - Sigma (G3893) - Western Blotting - rat cell and tissue lysates; Validation: Antibodypedia - https://www.antibodypedia.com/gene/3505/GFAP/antibody/80126/G3893

GFP - Millipore (AB16901) - Immunostaining - rat cells, mouse tissues: Validation: Manufacturer - https://www.emdmillipore.com/US/en/product/Anti-Green-

10. Eukaryotic cell lines

a. State the source of each eukaryotic cell line used.

HEK293 cells were obtained from ATCC (#CRL-1573)
HEK293T cells were obtained from ATCC (#CRL-11268)
Cos7 cells were obtained from ATCC (#CRL-1651)

b. Describe the method of cell line authentication used.

None of the cell lines used have been authenticated.

c. Report whether the cell lines were tested for mycoplasma contamination.

All cell lines tested negative for mycoplasma contamination.

d. If any of the cell lines used are listed in the database of commonly misidentified cell lines maintained by ICLAC, provide a scientific rationale for their use.

No commonly misidentified cell lines were used in this study.

Animals and human research participants

Policy information about studies involving animals; when reporting animal research, follow the ARRIVE guidelines

11. Description of research animals

Provide details on animals and/or animal-derived materials used in the study.

Experimental rats and mice included both males and females, between the ages of 0-21 days. The following strains were used:

Wildtype mice (CD1) - Charles River (022)
Wildtype rats (Sprague Dawley) - Charles River (SD-001)
Aldh1L1-EGFP (FVB/N) - MMRRC (#011015-UCD)
Glast-CreERT2 (C57BL/6 x SJL)F1 - Jackson Laboratories (012586)
Nlgn2 flox/flox (C57BL/6NTac) - Jackson Laboratories (025544)
Rosa26-td-Tomato (129S6/SvEvTac x C57BL/6NCrl)F1 - Jackson Laboratories (007908)

All animals, except dark reared mice, were kept under typical day/night conditions of 12-hours cycles. Dark reared mice were kept in total darkness from birth onward.

Policy information about studies involving human research participants

12. Description of human research participants

Describe the covariate-relevant population characteristics of the human research participants.

The study did not involve human research participants.

nature research

Corresponding author(s): Dr. Cagla Eroglu

☐ Initial submission ☒ Revised version ☐ Final submission

Flow Cytometry Reporting Summary

Form fields will expand as needed. Please do not leave fields blank.

Data presentation

For all flow cytometry data, confirm that:

☒ 1. The axis labels state the marker and fluorochrome used (e.g. CD4-FITC).

☒ 2. The axis scales are clearly visible. Include numbers along axes only for bottom left plot of group (a 'group' is an analysis of identical markers).

☒ 3. All plots are contour plots with outliers or pseudocolor plots.

☒ 4. A numerical value for number of cells or percentage (with statistics) is provided.

Methodological details

5. Describe the sample preparation.	NL2 cHET and cKO (includes GLAST-CreERT2 and Rosa-td-Tomato Reporter transgenes) mice were administered 0.6mg tamoxifen each on P10-11. On P21, the cortices from both hemispheres were microdissected, and papain digested to obtain a single cell suspension. The suspension was passed through a 40 micron strainer and run on a DiVaSorter Fluorescence Activated Cell Sorter (BD). td-Tomato positive cells were sorted and collected for RNA or gDNA. See Methods and Materials for further details.
6. Identify the instrument used for data collection.	BD DiVa Sorter
7. Describe the software used to collect and analyze the flow cytometry data.	No analysis of flow cytometry data was used.
8. Describe the abundance of the relevant cell populations within post-sort fractions.	Sample purity was determined by qPCR analysis of the astrocytic gene GFAP.
9. Describe the gating strategy used.	Gaiting was determined by the clear separation between td-Tomato positive cells and all other cells.

Tick this box to confirm that a figure exemplifying the gating strategy is provided in the Supplementary Information. ☒